Title:

Comparative genomics reveals signatures of distinct metabolic strategies and gene loss associated with *Hydra* immortality

Kaoruko Nojiri[1]†, Koryu Kin[1,2,3]†, Akimasa Someya[1,4], Tetsuo Kon[5], Koto Kon-Nanjo[5], Hiroshi Shimizu[6], Kazuharu Arakawa[7,8] and Etsuo A. Susaki[1,2,3,9]*

Affiliations:

[1]Faculty of Medicine, Juntendo University, 2-1-1 Hongo, Bunkyo-ku, Tokyo, 113-8421, Japan

[2]Department of Biochemistry and Systems Biomedicine, Juntendo University Graduate School of Medicine, 2-1-1 Hongo, Bunkyo-ku, Tokyo, 113-8421, Japan

[3]Nakatani Biomedical Spatialomics Hub, Juntendo University Graduate School of Medicine, 2-1-1 Hongo, Bunkyo-ku, Tokyo, 113-8421, Japan

[4]Juntendo University Graduate School of Pharmacy and Pharmaceutical Sciences, 6-8-1 Hinode, Urayasu, Chiba, 279-0013, Japan

[5]Department of Neurosciences and Developmental Biology, University of Vienna, Vienna, 1030, Austria

[6]National Institute of Genetics, 1111 Yata, Mishima, Shizuoka, 411-8540, Japan

[7]Institute for Advanced Biosciences, Keio University, 403-1 Nihonkoku, Daihoji, Tsuruoka, Yamagata, 997-0017, Japan

[8]Graduate School of Media and Governance, Keio University, 5322 Endo, Fujisawa, Kanagawa, 252-0882, Japan

[9]Institute for Quantum Life Science, National Institutes for Quantum Science and Technology, 4-9-1, Anagawa, Inage, Chiba, 263-0024, Japan

†These authors contributed equally to this work.

*corresponding to suishess-kyu@umin.ac.jp

Abstract

Hydra is a freshwater cnidarian genus that provides a unique comparative model for aging research, contrasting the immortal *H. vulgaris* with the aging-inducible *H. oligactis.* Here, we report a high-quality, chromosome-level genome assembly of *H. vulgaris* strain AEP.JNIG. Our assembly is comparable in quality to existing resources, facilitating the analysis of genomic diversity across laboratory strains. Epigenomic profiling revealed that gene-body hypermethylation correlates with transcriptional stability and the suppression of spurious transcription in evolutionary conserved genes, suggesting an epigenetic mechanism for genomic integrity. Furthermore, comparative genomics demonstrated that while *Hydra* conserves fundamental *Hallmarks of Aging* pathways, the immortal *H. vulgaris* paradoxically lacks canonical anti-aging genes (e.g., Klotho, NAMPT) found in the aging-inducible *H. oligactis*. Instead, *H. vulgaris* exhibits a distinct metabolic signature related to mitochondrial energy production and NTP synthesis. Collectively, our comparative genomics results suggest multiple potential mechanisms associated with the *H. vulgaris* immortality and the aging traits of *H. oligactis*, providing novel targets for future functional studies.

Introduction

Hydra is a freshwater cnidarian that can be maintained in the laboratory in mass culture [1–3]. Based on its distinctive traits including potent regenerative capacity and both sexual and asexual modes of reproduction, *Hydra* has been widely studied in fields such as stem cell biology, regeneration, and aging [4–6]. In particular, *Hydra vulgaris* is one of the few organisms in which negligible senescence has been demonstrated by long-term population monitoring of mortality and fertility [7,8]. Aging organisms exhibit progressive decline in physiological function and accumulation of pathological changes over time, characterized by an increase in mortality rate (Gompertz curve) [9,10]. On the other hand, *H. vulgaris* maintains a flat Gompertz curve [8], suggesting its immortality. This remarkable trait is thought to be supported by the continuous self-renewal capacity of its stem cell populations, regulated by genes including FoxO and TCF/β-catenin [11–13]. Interestingly, *H. oligactis*, another species within the *Hydra* genus, shows increased mortality and physiological deterioration after sexual reproduction when transferred to 10 °C [14]. This inducible aging phenotype has been attributed to the depletion of interstitial stem cells (ISCs) [15,16].

Hydra also constitutes an apparent exception to evolutionary theories of aging. These theories generally propose that organismal aging reflects an evolutionary trade-off that favors an energy-saving strategy, in which ensuring germline accuracy is essential, whereas maintaining somatic cell integrity is often a dispensable expenditure [17,18]. Therefore, whereas many long-lived species delay reproduction until later developmental stages, a pattern consistent with such theoretical predictions, *Hydra* attains sexual maturity early in life yet retains an extended lifespan [8].

What might be the origin of these unique aging traits in *Hydra*? While organismal aging is generally considered a complex process involving both genetic and environmental factors,

empirical evidence suggests that genetic components represent the primary determinant. Multiple findings support this proposition. First, maximum lifespan and aging patterns described by Gompertz curves show species-specific differences [10]. Second, multiple aging-related genes and pathways have been identified, such as Klotho, progeroid syndrome-related genes including DNA repair and nuclear integrity, and NAD^+-related pathways [22]. The *Hallmarks of aging* provides a comprehensive framework that summarizes genes and biological processes in aging [21]. Third, tissue and organismal aging is closely associated with the resilience of tissue stem cells, which is also determined by genomic information [22]. Lastly, a recent study demonstrated that the heritability of intrinsic life span is approximately 50%, suggesting that genetic control over longevity is comparable to other complex traits [23]. Therefore, comparative genomic analysis may provide critical insights into the genetic elements underlying the immortality observed in *H. vulgaris.*

While high-quality whole-genome assembly for the *H. vulgaris* strain AEP (North American strain) [24], originally established in North America [25], provides useful references for comparative genomics, they do not capture the full extent of intra-species genomic variation. Such variation may arise from spontaneously occurring mutants in laboratory cultures. Indeed, independent maintenance of laboratory populations or colonies can generally lead to genomic divergence across species [26,27]. In *H. vulgaris* 105 (formerly *H. magnipapillata*) maintained by asexual budding, the stem cells have accumulated mutations at even slightly higher rates than those in mammals, with some under positive selection [28]. Distinct types of transposable elements, such as the CR1 LINE element, are inserted into stem cell genomes, further contributing to genomic divergence [29,30]. These suggest that the *Hydra* genome can change over long-term cultures in laboratories, even when the animals reproduce asexually.

To avoid risks of overlooking population-specific variants that can affect phenotypic traits, at least two high-quality reference genomes from independently maintained *H. vulgaris* populations are desirable. To address this, we sequenced and assembled a

110 chromosome-level genome for the *H. vulgaris* AEP strain maintained at the National Institute
111 of Genetics, Mishima, Japan (hereafter *H. vulgaris* strain AEP.JNIG) [31], thereby expanding
112 available genomic resources for this species. We verified that *H. vulgaris* AEP.JNIG forms a
113 monophyletic group with other *H. vulgaris* strains, including AEP and 105, and is the most
114 closely related to AEP, while chromosomal analyses revealed substantial structural
115 differences, confirming genome-level divergence among populations. Building on these data,
116 we conducted a comparative analysis of aging-related genes and pathways using the
117 genomes of three *H. vulgaris* strains and the aging species *H. oligactis* [24]. By comparing
118 signaling pathways and genes tied to the *Hallmarks of Aging* [21], we identified gene sets that
119 differ between aging and non-aging species. From these comparisons, we characterized
120 genomic differences between *H. vulgaris* and representative aging animals, including *H.*
121 *oligactis*, and identified candidate genes potentially associated with *H. vulgaris* immortality.
122

Results

Chromosome-level genome assembly of *H. vulgaris* AEP.JNIG

The *H. vulgaris* population maintained at the National Institute of Genetics, Mishima, Japan (*H. vulgaris* AEP.JNIG, Fig 1A) was investigated. We independently sequenced and assembled the *H. vulgaris* AEP.JNIG genome as part of the Japanese *Hydra* resource; during the course of our work, a genome assembly of an *H. vulgaris* AEP strain maintained in the US was published [24]. The availability of both assemblies allowed us to evaluate the quality of the AEP.JNIG genome and to perform population-level comparisons of genomic variation.

The whole genome sequence of *H. vulgaris* AEP.JNIG genome was initially collected as the assemblies of Illumina paired-end reads and Nanopore long reads. We obtained 82,804,328,738 bp of paired-end short reads and 168,380,136,564 bp of Nanopore long reads with an N50 read length of 3,493 bp (Table 1). *De novo* assembly was performed using these sequences with Phased Error Correction and Assembly Tool (PECAT) [32] (see Materials and Methods for details). The initial genome assembly had a total size of 954,340,183 bp, consisting of 248 contigs. The longest contig was 61,504,050 bp, the contig N50 was 9,577,232 bp, the contig L50 was 30, and the GC content was 27.94%. (Table 2).

To construct a chromosome-level genome assembly, 398,191,666 Hi-C read pairs were generated from the same clone. We scaffolded the initial genome assembly using the Hi-C reads with HiC-pro [33] and YaHS [34] (see Materials and Methods for details). Fifteen chromosome-level scaffolds were obtained, each showing strong intra-chromosomal contact signals in the Hi-C contact map (Fig 1B). The total size of the final assembly was 922,069,947 bp, the largest scaffold was 86,117,336 bp, scaffold N50 was 63,895,935 bp, the contig L50 was 7, and the GC content was 27.88% (Table 2).

150 We evaluated the accuracy and completeness of the final genome assembly by searching for
151 sets of BUSCO (v 5.8.3) [35] using the metazoa odb10 database [36]. We identified 904
152 complete BUSCO genes out of 954 (94.7%), consisting of 879 single-copy genes (92.1%) and
153 25 duplicated genes (2.6%). 11 BUSCO genes were identified as fragmented (1.2%), and 39
154 BUSCO genes were missing (4.1%) (Fig 1C and Table 3). These assembly results are
155 comparable to those for the *H. vulgaris* AEP genome [24] (Tables 2 and 3), supporting the
156 sufficient quality of our genome assembly dataset. We further created gene models based on
157 this chromosome-level assembly and the transcriptome using BREAKER2 [37] and evaluated
158 BUSCO scores. This analysis identified 891 complete BUSCO genes out of 954 (93.4%),
159 consisting of 772 single-copy genes (80.9%) and 119 duplicated genes (12.5%). 14 BUSCO
160 genes were fragmented (1.5%), and 49 BUSCO genes were missing (5.1%). Again, these
161 results are also comparable to those for the AEP genome [24] (Table 4).
162
163 To further confirm the chromosome-level integrity of our AEP strain, we also performed
164 karyotyping (Fig 1D-F). Our microscopic observations predominantly indicate the karyotype of
165 2n = 30, with a few exceptions likely due to artifacts during sample preparations (Fig 1E, S1
166 Fig). Importantly, the absence of any karyotypes with 2n > 32 strongly suggests that *H. vulgaris*
167 AEP.JNIG does not possess extra chromosome pairs compared to other *H. vulgaris* strains.
168 Therefore, we conclude that the *H. vulgaris* AEP.JNIG has a karyotype of 2n = 30 (Fig 1F).
169

170 Comparison of *H. vulgaris* AEP.JNIG genome with AEP genome
171 revealed overall conservation of chromosomal structure

172
173 To determine the phylogenetic relationship between our strain and the other *Hydra* strains,
174 we performed species tree reconstruction using a large-scale phylogenomic dataset (a
175 multiple sequence alignment of 981,632 amino acid positions from 954 proteins) from 31
176 metazoan organisms including those of two other *H. vulgaris* strains and 2 holozoan protists

177 [24,29,38] (see Materials and Methods for details) (Fig 2A). The resulting species tree robustly
178 placed *H. vugaris* AEP.JNIG as the closest relative of the *H. vulgaris* AEP strain. Furthermore,
179 in order to see whether there is any strain closer to AEP.JNIG than AEP, we extracted four
180 genes (*COI*, *COII*, *EF1α*, *Cnnos1*) from the AEP.JNIG genome and made a phylogenetic tree
181 with other strains using a dataset previously published [31]. In all cases, *H. vulgaris* AEP.JNIG
182 formed a monophyletic group with *H. vulgaris* AEP (S2 Fig), further corroborating a close
183 phylogenetic relationship between *H. vulgaris* AEP.JNIG and *H. vulgaris* AEP.
184
185 To characterize the degree of genetic divergence between AEP and AEP.JNIG, we compared
186 their genomes using D-GENIES [39] and GENESPACE [40] (Fig 2B and 2C). The dot plot
187 from the genome alignment between these two genome sequences by D-GENIES revealed
188 prominent diagonal lines, indicating a high degree of collinearity between them (Fig 2B). The
189 ribbon plot from the gene syntenic analysis result by the GENESPACE demonstrated overall
190 correspondence at the chromosomal level (Fig 2C). We then used plotsr [41] and SyRI [42]
191 to visualize the detailed genomic structural variations such as inversions, translocations, and
192 duplications, and to quantify both structural and sequence-level differences including SNPs
193 and indels. In total, 954 syntenic regions were identified, covering 796 Mb of the AEP
194 assembly and 789 Mb of the AEP.JNIG assembly. In addition, 360 inversions (31.5 Mb) and
195 660 translocations (31.5 Mb) were also detected, along with numerous duplication events
196 (239 in the AEP and 2,073 in the AEP.JNIG) (Fig 2D and S3A Fig). At the sequence level,
197 1,833,472 SNPs, 648,211 insertions (5.4 Mb in total), and 261,207 deletions (4.7 Mb in total)
198 were identified (S3A Fig). Together, these results indicate that overall chromosomal
199 organization is largely conserved between the two strains, despite substantial accumulation
200 of sequence-level variation. Although we observed structural variations between the AEP and
201 AEP.JNIG assemblies, we cannot entirely rule out the possibility that some of these
202 differences arise from misassemblies in either genome. However, given the strong signals
203 observed in the Hi-C contact maps for both assemblies, such artifacts are likely minimal.

We also examined the transposable element (TE) landscape of the *H. vulgaris* AEP.JNIG assembly using Earl Grey (v6.3.3) [43]. Repetitive elements comprised 78.4% of the total genome (Table 5). DNA transposons were the most abundant class, representing 35.8% of the genome, and LINEs accounted for 15.2%. By contrast, LTR and Rolling-circle elements were relatively rare (1.0% and 1.0%, respectively). For direct comparison, we applied the same analysis to the *H. vulgaris* AEP assembly. The overall repeat content (77.7%) and element composition were similar between the two populations, although LINEs and Peneopes were slightly more abundant in AEP.JNIG (Table 6), indicating general consistency between the two assemblies. Despite slight differences in subfamily composition, TE landscape comparisons between the AEP.JNIG and AEP assemblies showed overall consistency (S3B and S3C Figs).

DNA Methylation within gene bodies contributes to transcriptional stability (homeostasis) of conserved genes in *H. vulgaris*

Leveraging the methylation signal in the Nanopore reads, we examined genome-wide mCpG distribution in *H. vulgaris* AEP.JNIG using Dorado (v0.7.1) and Modkit (v0.4.3) (see Materials and Methods). A mosaic methylation pattern was observed across the genome, with stably methylated and unmethylated regions interspersed. Centromeric regions identified by quarTeT (v1.2.5) [44] had low DNA methylation (Fig 3A).

We next compared methylation levels across genomic features. DNA methylation levels in promoters, exons, introns, and intergenic regions exhibited bimodal distributions, with distinct peaks corresponding to highly and weakly methylated regions. The methylation levels within gene regions were higher on average than those within promoter and intergenic regions (Fig 3B and S4A Fig). Repetitive elements also exhibited a bimodal methylation pattern. Among

231 repeat classes, LINEs and LTRs tended to be more highly methylated, a trend that is clearer
232 in the boxplots (Fig 3C and S4B Fig).
233
234 We further analyzed the relationship between DNA methylation and gene expression in our
235 dataset. We focused on conserved genes, defined as orthologs shared across the 33
236 holozoans (see Materials and Methods), because conserved genes have been reported to be
237 hypermethylated in multiple species, including cnidarians [45,46]. Consistent with these
238 reports, conserved genes in our data showed higher methylation than other genes (Fig 3D).
239 Conserved genes tended to be more highly expressed and exhibited less variation in
240 expression levels (Fig 3E and 3F), suggesting a link between methylation and stable gene
241 regulation. Finally, the ratio of transcription levels between exon 1 and downstream exons, a
242 measure of potential spurious transcription [47], was negatively correlated with exon
243 methylation, and this correlation was more pronounced for conserved genes than for other
244 genes (Fig 3G).
245
246 These results suggest that genomic methylation, particularly within gene bodies, may help
247 stabilize higher expression levels and suppress spurious transcription, especially in conserved
248 genes. This observation is consistent with findings in other cnidarians, such as coral [47].
249

250 Aging-related orthologs are conserved in *Hydra* comparable to other 251 aging model species

252
253 We then investigated aging-related orthologs in immortal *H. vulgaris* strains (105 [38], AEP
254 [24], and AEP.JNIG (this study)) and the aging species *H. oligactis* [24] in comparison with
255 other model organisms, including *Homo sapiens*, *Mus musculus*, *Drosophila melanogaster*,
256 and *Caenorhabditis elegans*. To reduce the impact of incomplete genome assemblies or gene

257 annotations, we integrated orthogroup information across three *H. vulgaris* strains, treating an
258 orthogroup as present when it was detected in any one of the strains.
259
260 First, we manually compiled a list of aging-related genes based on the *Hallmarks of Aging*
261 framework [21]. Specifically, genes explicitly mentioned in the original paper were directly
262 included. For hallmarks described at the level of signaling pathways rather than individual
263 genes, constituent genes were identified primarily using the KEGG Pathway database [48].
264 When pathways were not clearly defined or fully represented in KEGG, additional genes were
265 identified using the Gene Ontology (GO) database and relevant literature. The complete list of
266 genes is summarized in S1 Table. Subsequently, we used OrthoFinder [49] to construct
267 orthogroups based on predicted protein sequences derived from genome assemblies,
268 supplementing the analysis with BLAST searches. Finally, we examined the orthogroups
269 annotated with these aging-related genes. The presence of a sequence from a given species
270 within an orthogroup was taken as evidence that the species possesses the corresponding
271 gene.
272
273 Our analysis revealed that *Hydra* (both *H. vulgaris* and *H. oligactis*) conserve a substantial
274 proportion of genes associated with key aging-related pathways, such as autophagy,
275 proteostasis, DNA damage repair, mitochondrial quality control, stem cell regulation, insulin
276 receptor signaling, NAD signaling, and cGAS-STING signaling (Fig 4A and S5 Fig). For
277 instance, approximately 93% of the genes in the KEGG autophagy pathway (107/115) and
278 93% in the base excision repair pathway (39/42) were identified in *H. vulgaris* (see S2 Table
279 for details). These findings are consistent with previous reports [50–52] and suggest that the
280 fundamental mechanisms of aging mediated by these genes are likely conserved across
281 species, including the immortal *H. vulgaris* (Fig 4A).
282
283 Furthermore, a cross-species comparison of the total number of aging-related orthologs
284 revealed that *Hydra* shares a larger number of conserved orthologs with humans than do *D.*

285 *melanogaster* and *C. elegans* (Fig 4B). This indicates that *Hydra* has retained a highly
286 conserved repertoire of aging-related genes, despite its significant evolutionary distance from
287 traditional model organisms. Our results are supported by previous work using Reciprocal
288 Best Hit (RBH) analysis, which similarly showed that *H. vulgaris* possesses a greater number
289 of human orthologs than either *D. melanogaster* or *C. elegans* [53].
290
291 Therefore, these results substantiate the potential of *Hydra* as a model organism for aging
292 research, offering a unique opportunity to investigate conserved mechanisms of organismal
293 aging across the metazoan tree of life.
294

295 Comparative Analysis between *H. vulgaris* and *H. oligactis* reveals 296 aging-related orthologs

297
298 Finally, we conducted a comparative orthogroup analysis between *H. vulgaris* and *H. oligactis*,
299 particularly aiming at the identification of gene sets related to their aging or immortal traits. As
300 was in Fig 4, we used the integrated dataset for *H. vulgaris* orthogroups. To confirm the
301 absence of these orthogroups in each species, a BLAST search [54] was performed (see
302 Materials and Methods). This analysis revealed that *H. vulgaris* possessed 33 unique
303 orthogroups that were not detected in *H. oligactis*, while *H. oligactis* contained 65 unique
304 orthogroups (Fig 5A and 5B; S3 Table).
305
306 To explore their biological functions, we performed Gene Ontology (GO) enrichment, KEGG
307 pathway, and Reactome pathway analyses using clusterProfiler (v4.16.0) [55] (Figs 5C and
308 5D; S6 Fig; S4 Table). Intriguingly, terms related to oxidative phosphorylation (OXPHOS) were
309 enriched in both species (e.g., adjusted p-value = 4.60E-5 for *H. oligactis* and 9.72E-4 for *H.*
310 *vulgaris* in GO-biological processes (GO-BP); S4 Table). However, the specific genes
311 contributing to these terms are contrasted. Unique genes identified in the *H. oligactis* GO-BP

312 terms included α-synuclein (SNCA), mitochondrial deoxyguanosine kinase (DGUOK), and
313 components of complexes I (NDUFA10, MT-ND3), III (MT-CYB), IV (MT-CO2/CO3), and V
314 (MT-ATP6). In contrast, *H. vulgaris* uniquely possessed different components of complexes I
315 (NDUFA3/B7), III (UQCR10/11), and V (ATP5F1E). The analysis also revealed species-
316 specific terms regarding nucleic acid metabolic processes. For instance, *H. oligactis*-specific
317 orthogroups were enriched for GO-BP terms such as "purine deoxyribonucleoside
318 monophosphate metabolic process" (adjusted p-value = 8.29E-7), "purine nucleotide
319 metabolic process" (adjusted p-value = 2.99E-6), and "amide metabolic process" (adjusted p-
320 value = 3.71E-5) (Fig 5C and S4 Table). Conversely, in *H. vulgaris*, major GO-BP terms related
321 to NTP synthesis were enriched, such as "ATP biosynthetic process" (adjusted p-value =
322 9.72E-4) and "purine nucleoside triphosphate biosynthetic process" (adjusted p-value = 1.10E-
323 3) (Fig 5D and S4 Table). These contrasting results suggest species-specific characteristics
324 in energy production and metabolic processes.
325
326 We further narrowed our analysis to aging-related genes and pathways unique to each species.
327 By intersecting the species-specific orthogroups with the aging-related genes associated with
328 the *Hallmarks of Aging* (Fig 4 and S1 Table), we identified twelve [SNCA, FUT1/2, NAMPT,
329 BLVRB, SCD/SCD5, DPT, RBP3, IRG family (IRGC, IRGM), MPG, POLR2L, CD14, Klotho
330 family (KLB, LCT, LCTL, KL, GBA3)] and five [MON1A/1B, TOMM7, SS18 family (SS18,
331 SS18L1/2), PCLAF, RPS29] unique orthogroups for *H. oligactis* and *H. vulgaris*, respectively
332 (Fig 5B). Extending our comparative analysis to 29 other holozoan species revealed that the
333 twelve aging-related orthogroups identified in *H. oligactis* are largely conserved across these
334 taxa. Notably, both humans and mice possess the complete set of these twelve orthogroups
335 (Fig 5E). Conversely, the five orthogroups initially identified as unique to the immortal *H.*
336 *vulgaris* were found to be present in the other 29 species (Fig 5E). This suggests that these
337 orthogroups are unlikely to be the primary drivers of the immortal phenotype. Consequently,
338 we focused our subsequent investigation on the twelve *H. oligactis*-specific orthogroups.
339

340 These twelve orthogroups possess well-known functions in aging processes. α-synuclein
341 (SNCA) is a key molecule implicated in Parkinson's disease and mitochondrial oxidative
342 phosphorylation (OXPHOS) deficiency [56]. Nicotinamide adenine dinucleotide (NAD) is
343 widely recognized for its association with aging [57,58], and upregulation of genes involved in
344 NAD^+ biosynthesis accompanies lifespan extension [59]. Nicotinamide
345 phosphoribosyltransferase (NAMPT) functions as a rate-limiting enzyme in NAD^+ biosynthesis,
346 while biliverdin reductase B (BLVRB) is an NAD(P)H-dependent reductase involved in
347 antioxidant defense. Stearoyl-CoA desaturase (SCD/SCD5) has been linked to brain aging in
348 humans and mouse models of Alzheimer's disease through its role in the synthesis of
349 unsaturated fatty acids [60,61]. N-methylpurine DNA glycosylase (MPG) is involved in the
350 base excision repair (BER) pathway, potentially contributing to the DNA damage response
351 associated with aging, and is known to be upregulated in long-lived mammals [59,62]. The
352 presence of RNA polymerase II, I, and III subunit L (POLR2L) may be related to aging-
353 associated changes in transcriptional integrity [63,64]. Finally, it is intriguing that Klotho family
354 molecules are absent in *H. vulgaris*. *Klotho* is a well-known anti-aging gene whose knockout
355 in mice causes premature aging [65]. Although the absence of Klotho in the immortal *H.*
356 *vulgaris* appears inconsistent with the findings in mice, it suggests that the dependence on
357 Klotho-mediated pathways, such as phosphate and vitamin D metabolism, may be essential
358 for conferring the aging traits.
359
360 Collectively, these comparative analyses offer insights to address fundamental biological
361 questions: specifically, how *H. vulgaris* acquired the immortal trait (or conversely, lost the
362 aging trait) and what constitutes the essential genes and pathways underlying organismal
363 aging.
364

365 # Discussion

366

367 The purpose of this study was to establish a chromosome-level genome assembly and
368 accompanying epigenomic resources for *H. vulgaris* strain AEP.JNIG and offer insights into *H.*
369 *vulgaris* immortality through comparative genome analysis.

370

371 We established a chromosome-level genome assembly for *H. vulgaris* AEP.JNIG with quality
372 metrics comparable to the previously reported AEP strain (BUSCO: 94.7%; Scaffold N50: 63.9
373 Mb). Using the new high-quality genome assembly and accompanying gene annotations, we
374 clarified the relationship of our strain to other *H. vulgaris* strains. Our analyses demonstrate
375 that *H. vulgaris* AEP.JNIG forms a monophyletic group with *H. vulgaris* AEP. This close
376 relationship was consistently supported by both a phylogenomic dataset including multiple *H.*
377 *vulgaris* strains as well as single-gene analyses incorporating a broader taxonomic sampling
378 of *Hydra* laboratory strains and natural isolates.

379

380 Despite the phylogenetic proximity of the *H. vulgaris* AEP.JNIG and *H. vulgaris* AEP, through
381 detailed comparison between the two genomes, we detected a substantial accumulation of
382 SNPs and indels, along with numerous inversions and duplications. These genomic variations
383 likely reflect "laboratory drift" driven by long-term asexual reproduction, consistent with recent
384 findings that asexual lineages accumulate somatic mutations at high rates [28,66] and undergo
385 structural changes such as Robertsonian translocations [29]. Together, these findings
386 highlight substantial genomic diversity within the species, establishing the AEP.JNIG
387 assembly as a crucial resource that complements the existing *H. vulgaris* genomes.

388

389 In addition to the genome assembly, we provide foundational resources for epigenomic
390 analyses, including single-nucleotide 5-methylcytosine (5mC) calls and transposable element
391 (TE) annotations. Our Nanopore signal-based analysis identified a global methylation level of

392 19%, which is lower than the 27% previously estimated by bisulfite sequencing [67]. This
393 difference likely reflects the improved accuracy of signal-based detection, which is particularly
394 advantageous for analyzing repeat-rich genomes like *Hydra* [68]. We confirmed that the *H.*
395 *vulgaris* genome exhibits a characteristic methylation feature of invertebrates [69], where gene
396 bodies are hypermethylated while promoters and putative centromeres remain
397 hypomethylated. Further, we found the potential functional link between DNA methylation and
398 transcriptional stability. We observed that hypermethylation within gene bodies, particularly in
399 evolutionary conserved genes, correlates with high expression levels and low transcriptional
400 noise (spurious transcription). This finding suggests that gene body methylation serves as a
401 mechanism to maintain transcriptional fidelity and homeostasis in *Hydra*, aligning with findings
402 in other cnidarians such as corals [47,70]. The robust methylation-based stabilization of the
403 transcriptome, together with the loss of an RNA polymerase component (POLR2L) (Fig 5),
404 may represent a key machinery for *Hydra*'s negligible senescence. Given that epigenetic
405 alterations relates to the progress of aging, and that species-specific epigenetic signatures
406 have recently been shown to determine maximum lifespan in mammals [71], *Hydra* serves as
407 a unique model for investigating how an organism can escape these epigenetic constraints.
408
409 Finally, to interrogate the genetic basis of *Hydra* immortality, we employed a comparative
410 genomics approach contrasting the immortal *H. vulgaris* with the aging-inducible *H. oligactis*,
411 consistent with recent frameworks emphasizing comparisons between exceptional species
412 and related controls [72]. Our orthology analysis confirmed that *Hydra* shares a larger
413 repertoire of aging-related orthologs with humans than do traditional invertebrate models [53]
414 and highly conserves genes associated with the *Hallmarks of Aging*. This supports the view
415 that aging mechanisms are ancestral [73], suggesting *Hydra* achieves immortality by robustly
416 regulating these pathways rather than lacking them.
417
418 Intriguingly, however, we identified a counter-intuitive divergence: potential anti-aging genes
419 (e.g., Klotho, NAMPT, MPG) are unique to the aging *H. oligactis* and absent in the immortal

420 *H. vulgaris*. Additionally, metabolic signatures differed, with *H. vulgaris* enriched for ATP
421 synthesis pathways and *H. oligactis* for amide/purine metabolism pathways. We hypothesize
422 that *H. vulgaris*, inhabiting thermally stable environments [74], has optimized an efficient
423 energy metabolism that minimizes cellular damage, such as the synthesis of reactive oxygen
424 species. In contrast, the presence of metabolic regulators like Klotho in *H. oligactis*, living in a
425 cooler environment and sensitive to heat [74,75], implies complexity and trade-offs in the
426 metabolic system, consistent with an evolutionary aging theories such as antagonistic
427 pleiotropy [73]. Thus, *H. vulgaris* may maintain immortality by relying on a simpler homeostatic
428 system that avoids dependence on signaling pathways prone to age-dependent deterioration
429 and damage accumulation. From the viewpoint of evolutionary aging theories, it would be
430 intriguing to investigate mechanisms by which sexual reproduction triggers senescence in *H.*
431 *oligactis*, particularly within the context of the metabolic trade-offs imposed by its distinct
432 genetic background.
433
434 Several limitations of this study should be noted. First, our comparative analysis relies on
435 orthology with human aging-related genes defined by the *Hallmarks of Aging*. This approach
436 may overlook lineage-specific aging mechanisms unique to cnidarians. Additionally, despite
437 rigorous BLAST validation (e-value < 10^{-5}), the large evolutionary distance may lead to
438 potential undetected orthologs due to sequence divergence. Second, and most importantly,
439 the functional roles of the identified candidate genes (e.g., *H. oligactis*-specific genes) and the
440 causal link between DNA methylation and transcriptional stability remain to be experimentally
441 verified. Future studies employing functional assays, such as gene knockdown or transgenic
442 approaches, are essential to confirm the biological significance of these genomic findings for
443 *Hydra* aging and immortal traits.
444
445 In conclusion, our study provides an additional genomic resource comprising a new high-
446 quality, chromosome-level assembly of *H. vulgaris* AEP.JNIG, which facilitates the analysis of
447 genomic variation across independent laboratory populations. We also present a robust DNA

methylation profile derived from Nanopore sequencing signals, offering a foundation for future epigenetic studies in cnidarians. Furthermore, through comparative genomics, we offer novel insights into the potential genomic origins of *H. vulgaris* immortality, highlighting distinct metabolic strategies and the evolutionary trade-offs associated with anti-aging genes. Collectively, these resources and findings further establish *Hydra* as a robust and unique model for advancing the comparative biology of aging. To fully interrogate the questions regarding immortality in *Hydra*, more extensive analyses are required, including investigations into individual gene functions, the system-level input-output characteristics of entire pathways, and genetic loss- and gain-of-function assays.

Acknowledgements

We thank the lab members at DBSB Juntendo, particularly Y. Kumagai, Q. Su, K. Suzuki, A. Kanemitsu, K. Matsumoto, Y. Saito, and M. Ota for maintaining *Hydra* polyps and supporting the related experiments; K. Otomo for supporting chromosome imaging and karyotyping; Y. Wada and T.K. Suzuki for supporting computational resources. We also thank GeneBay, Inc. (Yokohama, Japan) for sequencing the *H. vulgaris* AEP.JNIG genome; K. Ikeo (National Institute of Genetics, Japan) for maintaining and providing Japanese hydra resource at NIG, S. Kuraku (National Institute of Genetics, Japan), R. Nakato (The University of Tokyo, Tokyo, Japan), and A. Watanabe (CyberomiX Inc., Kyoto, Japan) for fruitful suggestions about genome assembly and analysis. We would also like to thank S. Hamada, K. Hamada, and O. Koizumi (Fukuoka Women's University, Fukuoka, Japan) for his/her essential guidance in establishing *Hydra* in our laboratory and for providing protocols for its successful husbandry. We also extend our gratitude to Y. Takai (Institute for Advanced Biosciences, Keio University) for her technical assistance in Hi-C library preparation. We acknowledge the use of large language models (ChatGPT and Gemini) for English language proofreading and stylistic editing of the manuscript.

This study was supported by JSPS KAKENHI Grant-in-Aid for Scientific Research (B) (JP22H02824 to E.A.S.); JSPS KAKENHI for International Leading Research (23K20044 to E.A.S.); JST CREST (JPMJCR23B7 to E.A.S.); AMED Project for Promotion of Cancer Research and Therapeutic Evolution [P-PROMOTE] (JP25ama221610 to E.A.S.); Grants-in-Aid from Nakatani Foundation (to E.A.S.); JSPS KAKENHI Gran-in-Aid for Research Activity Start-up (24K23213 to K.K.); intramural Grant-in-Aid and Operating Costs Subsidies for Private Universities (to E.A.S.); research funds from the Yamagata Prefectural Government and Tsuruoka City, Japan (to K.A.); the JSPS Overseas Research Fellowships (to T.K.).

485 ## COI disclosure

486 There is no COI of all the authors regarding this study.

487

488 ## Data Availability

489 The genome assembly of *H. vulgaris* AEP.JNIG has been deposited in NCBI with BioProject
490 ID: PRJNA1413991 and BioSample accession: SAMN54890366.

491

492 ## Author contributions

493 E.A.S., K.N., K.K., and A.S. conceived and directed the study. H.S. maintained and provided
494 *H. vulgaris* AEP.JNIG resource. A.S. prepared the *H. vulgaris* AEP.JNIG genomic DNA and
495 RNA samples for sequencing. K.A. performed the Hi-C sequencing and analysis. K.K., T.K.,
496 K.K-N., and K.A. assembled the genome data. K.N. and K.K. performed the genomic
497 comparison between AEP.JNIG and AEP, whole-genome methylation analysis, and
498 comparative genome analysis. K.K. performed the karyotyping experiment. E.A.S., T.K., and
499 K.A. acquired funding. E.A.S., K.N., and K.K. mainly wrote the manuscript. All authors
500 discussed the results and commented on the manuscript.

501

502 # Materials and Methods

503

504 ## *Hydra* strain and culture

505 A *Hydra vulgaris* strain maintained as AEP at the Japan National Institute of Genetics (JNIG)
506 was acquired and cultured at Juntendo University using standard procedures. Briefly, the
507 animals were kept at 20ºC in the *Hydra* medium (1 mM Tris-HCl pH7.6, 1 mM $CaCl_2$, 1 mM
508 NaCl, 0.1 mM KCl, 0.1 mM $MgSO_4$) and were fed brine shrimp (*Artemia franciscana*) three
509 times a week.

510

511 ## Genome and RNA-Seq sequencing

512 For clean genomic DNA extraction, 100 polyps of *H. vulgaris* AEP.JNIG polyps were starved
513 for 10 days in the presence of antibiotics (50 µg/mL of ampicillin, rifampicin, neomycin, and
514 streptomycin) and herbicide (3-(3,4-dichlorophenyl)-1,1-dimethylurea (DCMU), 5 µM) to
515 eliminate possible algal contaminants. Whole genomic DNA was then extracted using WiZard
516 HMW DNA Extraction Kit (Promega, Cat. No. A2920) and sent for sequencing.

517

518 Nanopore sequencing was done using the instrument PromethION with the flowcell version
519 R.9.4.1. The basecalling was done using Guppy version 5.0
520 (https://nanoporetech.com/ja/software/other/guppy/). The qualities of the reads were
521 assessed using NanoPlot (https://github.com/wdecoster/NanoPlot) [76]. Short-read genome
522 sequencing libraries were also prepared from the extracted genomic DNA using the Truseq
523 DNA PCR-Free kit and 150 bp paired-end reads were sequenced on an Illumina NovaSeq
524 6000 platform.

525

526 The Hi-C sequencing library was prepared from 100 polyps of *H. vulgaris* AEP.JNIG with
527 EpiTect Hi-C Kit (Qiagen) according to manufacturer's instructions and was sequenced on
528 NovaSeq X Plus (Illumina) as 150 bp paired-end reads.

Karyotyping

Karyotyping was performed with minor modifications to a previously described protocol for various invertebrates [77]. To increase the number of proliferating cells [78], *H. vulgaris* AEP.JNIG polyps were heavily fed in the morning and, 12 hours later, treated with 0.1% nocodazole for 1 hour at room temperature. The organisms were then fixed in Carnoy's fixative (methanol : acetic acid = 3 : 1) for 30 minutes on ice. Fixed *Hydra* bodies were transferred to glass slides and incubated with a few drops (~30 μL) of 60% acetic acid for 5 minutes at room temperature. Siliconized coverslips prepared with Sigmacote (Sigma-Aldrich, Cat. No. SL2-25ML) were placed on top of the specimens, and the tissues were gently squashed by applying constant pressure for approximately 3 seconds to obtain a single layer of nuclei [77]. Slides were incubated overnight at 4 °C and subsequently chilled on dry ice for 10 minutes. Coverslips were removed using a blade while the slides remained on dry ice. After returning to room temperature, slides were gently rinsed twice with 1x phosphate-buffered saline (PBS), stained with 1 μg/mL 4′,6-diamidino-2-phenylindole (DAPI) for 5 minutes at room temperature, rinsed again with PBS, and mounted using ProLong Diamond (Invitrogen, Cat. No. P36965). Samples were imaged using an in-house spinning-disk confocal microscope (Nikon Eclipse Ti2-E equipped with a spinning-disk scanner with 100-μm-wide pinholes aligned with a Nipkow disk (CSU-MPϕ100; Yokogawa Electric) [79] and an oil-immersion lens (SR HP Apo TIRF 100XC Oil, numerical aperture [NA] = 1.49, Nikon)).

Genome assembly and annotation

The fastq files were assembled using the Phased Error Correction and Assembly Tool (PECAT) [32] with medaka (https://github.com/nanoporetech/medaka) as a polishing tool in the final phase of assembly.

555 For Hi-C scaffolding in *H. vulgaris* AEP.JNIG basecalled and demultiplexed reads totaling 119
556 Gbp were first filtered using fastp v0.19.4 [80] with -c and -g options, and the filtered reads
557 were processed with HiC Pro v3.1.0 [33]. Qualified reads were used to scaffold the assembly
558 using YAHS v1.2 [34] with default parameters. Scaffolds with length over 10 kbp were retained.
559 Contact map was generated using Juicer 2.20 pipeline [81]. The Hi-C contact map was curated
560 using the Juicebox v1.11.08 [81]. The final Hi-C contact map and genome assembly were
561 generated using the 'run-asm-pipeline-post-review.sh' script from the 3D-DNA pipeline [82].
562 The completeness of filtered genome assembly was evaluated by BUSCO v5.7.1 [35] with the
563 metazoa_odb10 dataset.
564
565 Prior to gene annotation, we soft-masked the assembled genome using RepeatModeler v2.0.2
566 and RepeatMasker v4.1.1 [83]. The soft-masked genomes were used to annotate protein-
567 coding genes using BRAKER v2.1.6 [37]. We used *H. vulgaris* AEP.JNIG whole-body RNA-
568 seq datasets as hints for annotation, mapped with HISAT2 v.2.2.1 [84].
569
570 The gene models annotated for the initial genome assembly were transferred to the final
571 assembly using Liftoff v1.6.3 [85]. Nine transcripts that were not transferred properly with the
572 initial Liftoff run were manually mapped to the new assembly using minimap2 [86] with the
573 splice mode, and the ORFs were predicted using Transdecoder [87].
574

575 ## Phylogenetic tree reconstruction

576 We constructed a proteome dataset of 31 metazoan and 2 unicellular holozoan organisms. A
577 workflow of constructing multiple sequence alignments based on the one described in [88]
578 was followed. Briefly, BUSCO v.5.8.0 [35] [35]was performed against each proteome using
579 metazoa_odb10. Single-copy genes were extracted from the BUSCO output of each species
580 and collected into individual FASTA files. These FASTA files were filtered first by the number
581 of species present in the dataset, with the threshold being 23 (i.e., less than 10 missing

species). PREQUAL v1.02 [89] was run with a posterior probability threshold of 0.95. Then MAFFT v7.525 [90] was used with the “-linsi” mode, without any other optional parameters. Divvier v1.01 [91] was used to remove regions of uncertain alignment (with the “-mincol 4 -divvygap” option), followed by trimming using trimAl v1.5 [92] (with the “-automated1” option). All the individual alignments were concatenated to create the final supermatrix used for the subsequent phylogenetic analyses. A maximum-likelihood phylogenetic tree was reconstructed using IQ-TREE2 v2.3.6 [93] under the "LG+C60+F+G" model, with branch support assessed by the ultrafast bootstrap method (1,000 replicates).

Molecular phylogenetic trees of *Hydra* strains based on mitochondrial and nuclear genes (*COI*, *COII*, *EF1α*, and *Cnnos1*) were reconstructed using the dataset used in [31]. Corresponding genes were retrieved from the *H. vulgaris* AEP.JNIG and the *H. vulgaris* AEP genomes and added to the original dataset. All trees were reconstructed with IQ-TREE2 under the best-fitting substitution models selected by ModelFinder (MFP option), with branch support assessed using the ultrafast bootstrap method.

Detection and visualization of genomic rearrangements between *H. vulgaris* AEP.JNIG and AEP assemblies

A dot plot was generated with D-GENIES [39] using the genomes of *H. vulgaris* AEP.JNIG and *H. vulgaris* AEP. Gene synteny plot was created using GENESPACE [40]. Structural rearrangements between the two assemblies were then detected by SyRI v1.7.1 [42] using *H. vulgaris* AEP as the reference and *H. vulgaris* AEP.JNIG as the query, and the results were visualized with plotsr [41]. Gene density was calculated based on *H. vulgaris* AEP gene models. Centromere positions were estimated from the repeat annotations identified by EDTA v2.2.2 [94] and processed with quarTeT (v1.2.5) [44], while repeat density was calculated using the output from Earl Grey (v6.3.3) [43].

Transposable element prediction

Transposable elements (TEs) in the *H. vulgaris* AEP and AEP. JNIG genomes were identified using Earl Grey v6.3.3 [43].

Methylation landscape analysis

The distribution of DNA methylation (mCpG) was detected from Nanopore raw signal data using Dorado (v0.7.1) (Oxford Nanopore Technologies: Dorado. https://github.com/nanoporetech/dorado.) and Modkit (v0.4.3) (Oxford Nanopore Technologies: Modkit. https://github.com/nanoporetech/modkit.). In Fig 3A the methylation frequency values output by Modkit were visualized using karyoploteR v1.32.0 [95]. Based on the gene model of *H. vulgaris* AEP.JNIG and the genomic locations of each TE class detected by Earl Grey v6.3.3 [43], mCpG/CpG ratios calculated for each genomic region using the "modkit stats" command in Fig 3B and 3C. Promoter regions were defined as the 2,000 bp upstream of the transcription start site (TSS), and regions that were neither within genes nor promoters were defined as intergenic regions. In Fig 3D and 3E, conserved genes were defined as orthologs shared across 33 species based on the output from Orthofinder. Fig 3F displays a scatter plot in which the x-axis represents the gene body–specific mCpG/CpG ratios obtained from "modkit stats", and the y-axis shows the corresponding RNA-seq expression levels (logTPM). The conserved genes shown in Fig 3E correspond to orthologs shared among all 33 species analyzed in Fig 5.

Spurious transcription analysis

Paired-end RNA-seq reads were aligned to the *H. vulgaris* AEP.JNIG genome using HISAT2 v2.2.1 [84] with default parameters. The resulting SAM files were converted to BAM format and sorted using SAMtools v1.23 [96]. Base-level read coverage across the genome was calculated using bedtools2 v2.31.1 [97] with the command "bedtools genomecov -d". Exon-level mean coverage was then calculated by mapping the exon BED file to the per-base

636 coverage BED file using “bedtools map -o mean”. For each gene, exon-level coverage values
637 were normalized by dividing by the coverage of the first exon (exon 1) of the same gene, ratios
638 were log-transformed using the natural logarithm for downstream comparisons. Exons with
639 zero or undefined coverage values were excluded. Genes were further annotated based on
640 two criteria: DNA methylation status and evolutionary conservation. Methylated genes were
641 defined as genes with mCpG/CpG ratios greater than 60%, whereas conserved genes were
642 defined as genes belonging to orthogroups shared across all 33 species. This produced four
643 groups: conserved–hypermethylated, conserved–hypomethylated, nonconserved–
644 hypermethylated, and nonconserved–hypomethylated. For each exon position (exons 1–6),
645 the mean log-transformed coverage ratio was calculated separately for each of the four gene
646 groups.
647

648 Conservation of aging related orthologous comparative Analysis of 649 Orthologous Groups in *Hydra oligactis* and *Hydra vulgaris*

650 Orthologs were identified using OrthoFinder(v2.5.5) [49]. Protein sequences from 33 species
651 were used as input data, and the topology of the phylogenetic tree was based on the study by
652 [98,99], which was then confirmed by our own phylogenomic analysis. Details are provided on
653 the official GitHub repository (https://github.com/nojiruko/H_vulgaris_AEP.JNIG). Each
654 orthogroup was annotated using human protein sequences as references, and the
655 correspondence table of gene name and Protein stable ID obtained from Ensembl BioMart
656 (https://www.ensembl.org/info/data/biomart/index.html) was used. Additionally, we compared
657 the presence or absence of orthogroups between *Hydra oligactis* and *Hydra vulgaris, made a*
658 *list of ortholog groups differentially present,* and performed GO, KEGG, and Reactome
659 enrichment analyses. Enrichment analyses were conducted using ClusterProfiler v4.14.4 [55]
660 and ReactomePA v1.50.0 [100], with the human database referenced from org.Hs.eg.db
661 v3.20.0 [101].

662 Genes involved in aging-related pathways were determined based on López-Otín, C. *et al*.
663 (2023) [21]. First, we manually compiled a list of aging-related genes based on the *Hallmarks*
664 *of Aging* framework [21]. Specifically, genes explicitly mentioned in the original paper were
665 directly included. For hallmarks described at the level of signaling pathways rather than
666 individual genes, constituent genes were identified primarily using the KEGG Pathway
667 database [48]. When pathways were not clearly defined or fully represented in KEGG,
668 additional genes were identified using the Gene Ontology (GO) database and relevant
669 literature. The complete list of genes is summarized in S1 Table. For orthogroups showing
670 differential conservation between *H. oligactis* and *H. vulgaris*, we performed BLASTP (protein
671 query vs protein database) searches to verify whether homologous sequences were present
672 in the proteome of the other species, using an e-value threshold of 10^{-5}. Specifically, for
673 orthogroups identified in *H. oligactis* but absent in *H. vulgaris*, *H. oligactis* protein sequences
674 were used as BLASTP queries against the locally created proteome databases of *H. vulgaris*
675 AEP and *H. vulgaris* AEP.JNIG. Conversely, for ortholog groups found in *H. vulgaris* but
676 absent in *H.oligactis*, *H. vulgaris* AEP.JNIG protein sequences were queried against the locally
677 created proteome database of *H. oligactis*. Orthogroups present in at least one *H. vulgaris*
678 strain but not detected in *H. oligactis* were defined as *H. vulgaris*-unique. Orthogroups absent
679 from all three *H. vulgaris* strains but present in *H. oligactis* were defined as *H. oligactis*-unique.
680

681 # Figure legends

682

683 **Figure 1.** Chromosome-level genome assembly of *H. vulgaris* AEP.JNIG.

684 **(A)** Picture of cultured *H. vulgaris* AEP.JNIG. Scale bar: 1 mm.

685 **(B)** Hi-C contact map, showing the 15 chromosome-level scaffolds of *H. vulgaris* AEP.JNIG.
686 Darker red indicates genomic regions with higher contact frequencies, reflecting closer spatial
687 proximity.

688 **(C)** Snail plot demonstrating the quality of our genome assembly.

689 **(D)** A representative image of metaphase chromosomes in *H. vulgaris* AEP.JNIG stained with
690 DAPI and observed with a scanning disk confocal microscope. Scale bar: 5 μm.

691 **(E)** Histogram of karyotypes observed in this study. Chromosome counts show a distinct peak
692 at 2n = 30. The absence of nuclei with 2n > 32 supports a chromosome number of 30,
693 consistent with our and other genome assembly data.

694 **(F)** Karyogram of *Hydra vulgaris* AEP.JNIG showing 15 chromosomes.

695

696 **Figure 2.** Comparison of *H. vulgaris* AEP and *H. vulgaris* AEP.JNIG genome assemblies

697 **(A)** Maximum likelihood phylogenetic analysis of a phylogenomic dataset constructed from 33
698 holozoan proteomes shows that *H. vulgaris* AEP and *H. vulgaris* AEP.JNIG form a
699 monophyletic clade. Nodes marked with black dots (●) indicate 100% ultrafast bootstrap
700 support, while other nodes were labelled with their corresponding ultrafast bootstrap support
701 values. The scale bar represents 0.5 amino acid substitutions per site.

702 **(B)** A dot-plot created with D-GENIES shows that the genome of *H. vulgaris* JNIG (on the y-
703 axis) aligns well with that of *H. vulgaris* AEP genome [24] (on the x-axis, indicating a high
704 genomic similarity between the two strains. The color indicates the identity score as shown in
705 the legend on the right.

706 **(C)** Gene synteny plot generated by GENESPACE showing conserved synteny of orthologous
707 genes between the AEP and AEP.JNIG genomes. The AEP.JNIG chromosomes are shown

708 at the top and the AEP chromosomes at the bottom. Chromosome numbering and sequence
709 strand orientation were standardized to match previously published genome assemblies.
710 **(D)** Visualization of syntenic regions and structural rearrangements between chromosomes
711 from *H. vulgaris* AEP and *H. vulgaris* AEP.JNIG genomes. Annotation tracks for four genomic
712 features (number of SNPs, genes, repetitive regions and centromeres) were included using
713 optional parameters above the lines showing the chromosomes of each strain. In the
714 annotation tracks, higher values indicate greater density.
715
716 **Figure 3.** DNA Methylation within Gene Bodies Contributes to Transcriptional Stability
717 (Homeostasis) of Conserved Genes in *H. vulgaris*
718 **(A)** Global pattern of DNA methylation in *H. vulgaris* AEP.JNIG genome showed that
719 centromeric regions had low DNA methylation. The top track shows the methylation frequency
720 (the probability that each base is methylated). The second track indicates the predicted
721 centromere positions in red, which was identified by quarTeT (v 1.2.5) [44] .
722 **(B)** Methylation level across each genomic region. The gene region was further analyzed by
723 dividing exon and intron regions.
724 **(C)** Methylation level of each repetitive region. The colors correspond to those used in Fig 3A.
725 **(D)** Boxplots of gene-body methylation levels in conserved (purple) and other (gray) genes.
726 Differences were significant (Mann-Whitney U test, $p < 1\times10^{-4}$).
727 **(E)** Boxplots showing expression levels in the conserved (purple) and the other (gray) genes.
728 Differences were significant (Mann-Whitney U test, $p < 1\times10^{-4}$).
729 **(F)** Relationship between DNA methylation levels in gene bodies and gene expression. Purple
730 dots indicate conserved genes, and gray dots indicate other genes. Values indicate the
731 coefficient variation of each group's logTPM.
732 **(G)** Spurious transcription in gene bodies is significantly lower in the conserved and highly
733 methylated genes (normalized by exon length for the logFC). The y axis shows the natural
734 logarithm of the coverage fold change (FC) of exons 1 to 6 versus exon 1, with lower values
735 meaning less spurious transcription.

736

737 **Figure 4.** Conservation of aging-related orthologs in *Hydra*

738 **(A)** Conservation of orthologs related to the *Hallmarks of Aging*. The vertical axis lists
739 representative aging-related pathways (defined as KEGG terms). Each pathway was
740 extracted from the 12 hallmarks of aging proposed in 2023 [21]. Genes including each pathway
741 were listed as described in the Materials and Methods and summarized in S4 Table. Numbers
742 inside the circles indicate the number of conserved orthologs, and the circle size corresponds
743 to the number of conserved orthologs. The *Hydra* genus is highlighted in purple.

744 (**B)** Bar plot showing the total number of conserved aging-related orthologs identified in each
745 species. The y-axis represents the number of orthogroups. The *Hydra* genus is highlighted in
746 purple.

747

748 **Figure 5.** Comparative Analysis between *H. vulgaris* and *H. oligactis*

749 (**A)** Schematic diagram illustrating the method used to identify *H. vulgaris*- and *H. oligactis*-
750 specific aging-related genes. A part of figure materials was prepared using biorender.com
751 (permission No. JK2989SSUB).

752 **(B)** Twelve genes are present in *H. oligactis* but absent in *H. vulgaris*, whereas five genes are
753 present in *H. vulgaris* but not in *H. oligactis*. A total of 7,684 genes is shared between the two
754 species. Note that only genes annotated based on homology to human genes were included
755 in this analysis. We referred to the original article [21] for the factors of *Hallmarks of Aging*.
756 Icons for the analyzed species were referred to from PhyloPic (https://www.phylopic.org/)
757 under Creative Commons license.

758 **(C)** Gene Ontology (GO) enrichment analysis for biological processes was performed using
759 65 orthogroups present in *H. oligactis* but absent in *H. vulgaris*. The y-axis shows the top 13
760 significantly enriched GO terms. The x-axis represents the gene ratio, defined as the
761 proportion of input genes associated with each term. The color intensity of the bars indicates
762 the adjusted p-value (p.adj), with darker colors representing higher statistical significance.

763 **(D)** The same analysis was performed for 33 orthogroups present in *H. vulgaris* but absent in
764 *H. oligactis*.
765 **(E)** Orthogroups specific to *H. oligactis* (65 OGs) and *H. vulgaris* (33 OGs) were screened
766 across 33 species to identify those involved in aging-related pathways defined in this study
767 based on the *Hallmarks of Aging*. The final list of genes is shown on the x-axis. The y-axis
768 represents the species included in this analysis, ordered by phylogeny. Dots indicate the
769 presence of the corresponding gene in each species, while blanks indicate absence. The
770 colors at the top represent the *Hallmarks of Aging* categories assigned to each gene. The
771 names of each category and the specific terms included in them are shown on the right.
772
773 **Table 1.** Summary of the genome sequencing
774 **Table 2.** Assembly statistics of the *H. vulgaris* genome.
775 **Table 3.** BUSCO score from the genome assembly
776 **Table 4.** BUSCO score from the gene model
777 **Table 5.** Composition of TEs identified by Earl Grey in the genomes of *H. vulgaris* AEP.
778 JNIG.
779 **Table 6.** Composition of TEs identified by Earl Grey in the genomes of *H. vulgaris* AEP.
780

Supplementary figure legends

Figure S1. Karyotyping Data

Karyotype of *H. vulgaris* AEP.JNIG. A total of 30 nuclei samples were examined, and the number of chromosomes were counted. The number in yellow indicates the karyotype (2n) of the corresponding image. Scale Bar = 5 μm.

Figure S2. Molecular phylogenetic trees of *Hydra* strains based on mitochondrial and nuclear genes.

Trees were reconstructed using IQ-TREE2 with best-fitting models selected by ModelFinder (MFP option). Branch support was evaluated using the ultrafast bootstrap method. *H. vulgaris* AEP.JNIG and *H. vulgaris* AEP sequences are shown in red and blue, respectively. *H. vulgaris* AEP sequences from [31] ("*Hydra vulgaris* AEP") and those derived from the *H. vulgaris* AEP genome [24] ("*Hydra vulgaris* AEP_genome") [24]are indicated by distinct labels. Numbers at nodes represent ultrafast bootstrap support values. Scale bars represent 0.05 nucleotide substitutions per site.

(A) A molecular phylogenetic tree based on *COI*.

(B) A molecular phylogenetic tree based on *COII*.

(C) A molecular phylogenetic tree based on *EF1α*.

(D) A molecular phylogenetic tree based on *Cnnos1*.

Figure S3. Comparison of the transposable elements between AEP.JNIG and AEP

(A) Quantitatively assessed structural and sequence variation identified by SyRI. Structural and sequence variations were identified using SyRI with the AEP assembly as the reference and the AEP.JNIG assembly as the query. Sequence lengths are shown in megabases (Mb).

(B) Transposable elements (TEs) landscape showing the distribution of repetitive elements in the genome based on Kimura distance. The x-axis represents the Kimura 2-Parameter

808 distance, where lower scores indicate more recent insertions into the genome, while higher
809 scores correspond to older insertions. The y-axis shows the total number of base pairs
810 contributed by each class of transposable elements at each divergence level. The pie chart
811 shows the components and proportions of repetitive sequences in the *H. vulgaris* AEP.JNIG
812 genome.
813 **(C)** Transposable elements (TEs) landscape of *H. vulgaris* AEP, as in B.
814
815 **Figure S4.** The methylation level of *H. vulgaris* AEP depicted as box plots, related to Fig 3B
816 and 3C.
817 **(A)** The box plot of the methylation level across each genomic region, corresponding to Fig
818 3B.
819 **(B)** The box plot of the methylation level of each repetitive region, corresponding to Fig 3C.
820
821 **Figure S5.** Conservation of aging-related orthologs in *Hydra*, related to Fig 4.
822 Conservation of orthologs related to the *Hallmarks of Aging*, as in Fig 4A. The vertical axis
823 lists representative aging-related pathways (defined as GO terms).
824
825 **Figure S6.** Enrichment analysis results of *H. oligactis*-specific and *H. vulgaris*-specific
826 orthogroups using multiple annotation databases.
827 **(A)** Results of Gene Ontology – Cellular Component (GO-CC) terms.
828 **(B)** Results of Gene Ontology – Molecular Function (GO-MF) terms.
829 **(C)** Results of KEGG pathway terms.
830 **(D)** Results of Reactome pathway terms.
831 In each panel, *H. oligactis*-specific orthogroups are shown on the left, whereas *H. vulgaris*-
832 specific orthogroups are shown on the right.
833

834 **Table S1.** Complete list of aging-related genes included in this study. This table provides the
835 full list of aging-related genes identified in this study. For each gene, the second column
836 indicates the associated aging-related pathways, and the third column classifies the gene
837 according to the *Hallmarks of Aging*.
838
839 **Table S2.** Summary of the conservation of aging-related genes for each pathway, related to
840 Fig 4 and Fig S5**.**
841 This table provides an overview of the conservation of aging-related genes identified through
842 GO, KEGG and literature-based searches based on the *Hallmarks of Aging* [21]. The first
843 column lists aging-related pathways, and the subsequent columns show the number of
844 conserved orthogroups in each species.
845
846 **Table S3**. Lists of orthogroups specific to *H. oligactis* (65 OGs) and *H. vulgaris* (33 OGs).
847 Each row corresponds to one orthogroup. The second column shows annotations with the
848 corresponding human genes. The third column shows the pathway annotation for each
849 aging-related gene.
850
851 **Table S4**. Enrichment analysis of the 33 *H. vulgaris* specific orthogroups and 65 *H. oligactis*
852 specific orthogroups. Significantly enriched terms (adjusted p-value < 0.05) are shown. Ten
853 files are provided, corresponding to all combinations of species-specific gene sets (*H.*
854 *oligactis*-specific and *H. vulgaris*-specific) and annotation databases (GO biological process,
855 GO cellular component, GO molecular function, KEGG, and Reactome).
856

857 # References

858

859 1. Klimovich A, Wittlieb J, Bosch TCG. Transgenesis in Hydra to characterize gene
860 function and visualize cell behavior. Nat Protoc. 2019;14: 2069–2090.
861 2. Galliot B. Hydra, a fruitful model system for 270 years. Int J Dev Biol. 2012;56: 411–423.
862 3. Loomis WF, Lenhoff HM. Growth and sexual differentiation of hydra in mass culture. J
863 Exp Zool. 1956;132: 555–573.
864 4. Holstein TW. The Hydra stem cell system - Revisited. Cells Dev. 2023;174: 203846.
865 5. Vogg MC, Galliot B, Tsiairis CD. Model systems for regeneration: Hydra. Development.
866 2019;146: dev177212.
867 6. Tomczyk S, Fischer K, Austad S, Galliot B. Hydra, a powerful model for aging studies.
868 Invertebr Reprod Dev. 2015;59: 11–16.
869 7. Martínez DE. Mortality patterns suggest lack of senescence in hydra. Exp Gerontol.
870 1998;33: 217–225.
871 8. Schaible R, Scheuerlein A, Dańko MJ, Gampe J, Martínez DE, Vaupel JW. Constant
872 mortality and fertility over age in Hydra. Proc Natl Acad Sci U S A. 2015;112: 15701–
873 15706.
874 9. Finch CE, Pike MC, Witten M. Slow mortality rate accelerations during aging in some
875 animals approximate that of humans. Science. 1990;249: 902–905.
876 10. Jones OR, Scheuerlein A, Salguero-Gómez R, Camarda CG, Schaible R, Casper BB, et
877 al. Diversity of ageing across the tree of life. Nature. 2014;505: 169–173.
878 11. Boehm A-M, Khalturin K, Anton-Erxleben F, Hemmrich G, Klostermeier UC, Lopez-
879 Quintero JA, et al. FoxO is a critical regulator of stem cell maintenance in immortal
880 Hydra. Proc Natl Acad Sci U S A. 2012;109: 19697–19702.
881 12. Hemmrich G, Khalturin K, Boehm A-M, Puchert M, Anton-Erxleben F, Wittlieb J, et al.
882 Molecular signatures of the three stem cell lineages in hydra and the emergence of
883 stem cell function at the base of multicellularity. Mol Biol Evol. 2012;29: 3267–3280.

884 13. Gufler S, Artes B, Bielen H, Krainer I, Eder M-K, Falschlunger J, et al. β-Catenin acts in
885 a position-independent regeneration response in the simple eumetazoan Hydra. Dev
886 Biol. 2018;433: 310–323.
887 14. Yoshida K, Fujisawa T, Hwang JS, Ikeo K, Gojobori T. Degeneration after sexual
888 differentiation in hydra and its relevance to the evolution of aging. Gene. 2006;385: 64–
889 70.
890 15. Sun S, White RR, Fischer KE, Zhang Z, Austad SN, Vijg J. Inducible aging in Hydra
891 oligactis implicates sexual reproduction, loss of stem cells, and genome maintenance as
892 major pathways. GeroScience. 2020;42: 1119–1132.
893 16. Tomczyk S, Suknovic N, Schenkelaars Q, Wenger Y, Ekundayo K, Buzgariu W, et al.
894 Deficient autophagy in epithelial stem cells drives aging in the freshwater cnidarian
895 Hydra. Development. 2020;147: dev177840.
896 17. Kirkwood TB. Evolution of ageing. Nature. 1977;270: 301–304.
897 18. Hamilton WD. The moulding of senescence by natural selection. J Theor Biol. 1966;12:
898 12–45.
899 19. Nabeshima Y-I. Klotho: a fundamental regulator of aging. Ageing Res Rev. 2002;1:
900 627–638.
901 20. Lombard DB, Chua KF, Mostoslavsky R, Franco S, Gostissa M, Alt FW. DNA repair,
902 genome stability, and aging. Cell. 2005;120: 497–512.
903 21. López-Otín C, Blasco MA, Partridge L, Serrano M, Kroemer G. Hallmarks of aging: An
904 expanding universe. Cell. 2023;186: 243–278.
905 22. Rando TA, Jones DL. Regeneration, rejuvenation, and replacement: Turning back the
906 clock on tissue aging. Cold Spring Harb Perspect Biol. 2021;13: a040907.
907 23. Shenhar B, Pridham G, De Oliveira TL, Raz N, Yang Y, Deelen J, et al. Heritability of
908 intrinsic human life span is about 50% when confounding factors are addressed.
909 Science. 2026;391: 504–510.
910 24. Cazet JF, Siebert S, Little HM, Bertemes P, Primack AS, Ladurner P, et al. A
911 chromosome-scale epigenetic map of the Hydra genome reveals conserved regulators

912 of cell state. Genome Res. 2023;33: 283–298.
913 25. Martínez DE, Iñiguez AR, Percell KM, Willner JB, Signorovitch J, Campbell RD.
914 Phylogeny and biogeography of Hydra (Cnidaria: Hydridae) using mitochondrial and
915 nuclear DNA sequences. Mol Phylogenet Evol. 2010;57: 403–410.
916 26. Chebib J, Jackson BC, López-Cortegano E, Tautz D, Keightley PD. Inbred lab mice are
917 not isogenic: genetic variation within inbred strains used to infer the mutation rate per
918 nucleotide site. Heredity (Edinb). 2021;126: 107–116.
919 27. Farslow JC, Lipinski KJ, Packard LB, Edgley ML, Taylor J, Flibotte S, et al. Rapid
920 Increase in frequency of gene copy-number variants during experimental evolution in
921 Caenorhabditis elegans. BMC Genomics. 2015;16: 1044.
922 28. Sahm A, Riege K, Groth M, Bens M, Kraus J, Fischer M, et al. Hydra has mammal-like
923 mutation rates facilitating fast adaptation despite its nonaging phenotype. Genome Res.
924 2024;34: 2217–2228.
925 29. Kon-Nanjo K, Kon T, Yu TC-TK, Rodriguez-Terrones D, Falcon F, Martínez DE, et al.
926 The dynamic genomes of Hydra and the anciently active repeat complement of animal
927 chromosomes. Genome Biol. 2025;26: 186.
928 30. Wong WY, Simakov O, Bridge DM, Cartwright P, Bellantuono AJ, Kuhn A, et al.
929 Expansion of a single transposable element family is associated with genome-size
930 increase and radiation in the genus Hydra. Proc Natl Acad Sci U S A. 2019;116: 22915–
931 22917.
932 31. Kawaida H, Shimizu H, Fujisawa T, Tachida H, Kobayakawa Y. Molecular phylogenetic
933 study in genus Hydra. Gene. 2010;468: 30–40.
934 32. Nie F, Ni P, Huang N, Zhang J, Wang Z, Xiao C, et al. De novo diploid genome
935 assembly using long noisy reads. Nat Commun. 2024;15: 2964.
936 33. Servant N, Varoquaux N, Lajoie BR, Viara E, Chen C-J, Vert J-P, et al. HiC-Pro: an
937 optimized and flexible pipeline for Hi-C data processing. Genome Biol. 2015;16: 259.
938 34. Zhou C, McCarthy SA, Durbin R. YaHS: yet another Hi-C scaffolding tool.
939 Bioinformatics. 2022;39. doi:10.1101/2022.06.09.495093

35. Manni M, Berkeley MR, Seppey M, Simão FA, Zdobnov EM. BUSCO update: Novel and streamlined workflows along with broader and deeper phylogenetic coverage for scoring of eukaryotic, prokaryotic, and viral genomes. Mol Biol Evol. 2021;38: 4647–4654.
36. Kriventseva EV, Kuznetsov D, Tegenfeldt F, Manni M, Dias R, Simão FA, et al. OrthoDB v10: sampling the diversity of animal, plant, fungal, protist, bacterial and viral genomes for evolutionary and functional annotations of orthologs. Nucleic Acids Res. 2019;47: D807–D811.
37. Brůna T, Hoff KJ, Lomsadze A, Stanke M, Borodovsky M. BRAKER2: automatic eukaryotic genome annotation with GeneMark-EP+ and AUGUSTUS supported by a protein database. NAR Genom Bioinform. 2021;3: lqaa108.
38. Chapman JA, Kirkness EF, Simakov O, Hampson SE, Mitros T, Weinmaier T, et al. The dynamic genome of Hydra. Nature. 2010;464: 592–596.
39. Cabanettes F, Klopp C. D-GENIES: dot plot large genomes in an interactive, efficient and simple way. PeerJ. 2018;6: e4958.
40. Lovell JT, Sreedasyam A, Schranz ME, Wilson M, Carlson JW, Harkess A, et al. GENESPACE tracks regions of interest and gene copy number variation across multiple genomes. Elife. 2022;11. doi:10.7554/eLife.78526
41. Goel M, Schneeberger K. Plotsr: Visualizing structural similarities and rearrangements between multiple genomes. Bioinformatics. 2022;38: 2922–2926.
42. Goel M, Sun H, Jiao W-B, Schneeberger K. SyRI: finding genomic rearrangements and local sequence differences from whole-genome assemblies. Genome Biol. 2019;20: 277.
43. Baril T, Galbraith J, Hayward A. Earl Grey: A fully automated user-friendly transposable element annotation and analysis pipeline. Mol Biol Evol. 2024;41. doi:10.1093/molbev/msae068
44. Lin Y, Ye C, Li X, Chen Q, Wu Y, Zhang F, et al. quarTeT: a telomere-to-telomere toolkit for gap-free genome assembly and centromeric repeat identification. Hortic Res. 2023;10: uhad127.

968 45. Zhang X, Jacobs D. A broad survey of gene body and repeat methylation in Cnidaria
969 reveals a complex evolutionary history. Genome Biol Evol. 2022;14.
970 doi:10.1093/gbe/evab284
971 46. Sarda S, Zeng J, Hunt BG, Yi SV. The evolution of invertebrate gene body methylation.
972 Mol Biol Evol. 2012;29: 1907–1916.
973 47. Li Y, Liew YJ, Cui G, Cziesielski MJ, Zahran N, Michell CT, et al. DNA methylation
974 regulates transcriptional homeostasis of algal endosymbiosis in the coral model
975 Aiptasia. Sci Adv. 2018;4: eaat2142.
976 48. Kanehisa M, Goto S. KEGG: kyoto encyclopedia of genes and genomes. Nucleic Acids
977 Res. 2000;28: 27–30.
978 49. Emms DM, Kelly S. OrthoFinder: phylogenetic orthology inference for comparative
979 genomics. Genome Biol. 2019;20: 238.
980 50. Pascual-Torner M, Carrero D, Pérez-Silva JG, Álvarez-Puente D, Roiz-Valle D,
981 Bretones G, et al. Comparative genomics of mortal and immortal cnidarians unveils
982 novel keys behind rejuvenation. Proc Natl Acad Sci U S A. 2022;119: e2118763119.
983 51. Barve A, Galande AA, Ghaskadbi SS, Ghaskadbi S. DNA repair repertoire of the
984 enigmatic hydra. Front Genet. 2021;12: 670695.
985 52. Chera S, Buzgariu W, Ghila L, Galliot B. Autophagy in Hydra: a response to starvation
986 and stress in early animal evolution. Biochim Biophys Acta. 2009;1793: 1432–1443.
987 53. Wenger Y, Galliot B. Punctuated emergences of genetic and phenotypic innovations in
988 eumetazoan, bilaterian, euteleostome, and hominidae ancestors. Genome Biol Evol.
989 2013;5: 1949–1968.
990 54. Altschul SF, Gish W, Miller W, Myers EW, Lipman DJ. Basic local alignment search tool.
991 J Mol Biol. 1990;215: 403–410.
992 55. Wu T, Hu E, Xu S, Chen M, Guo P, Dai Z, et al. clusterProfiler 4.0: A universal
993 enrichment tool for interpreting omics data. Innovation (Camb). 2021;2: 100141.
994 56. Miwa S, Kashyap S, Chini E, von Zglinicki T. Mitochondrial dysfunction in cell
995 senescence and aging. J Clin Invest. 2022;132. doi:10.1172/JCI158447

996 57. Imai S-I, Guarente L. NAD+ and sirtuins in aging and disease. Trends Cell Biol.
997 2014;24: 464–471.
998 58. Imai S-I. The NAD World 2.0: the importance of the inter-tissue communication
999 mediated by NAMPT/NAD+/SIRT1 in mammalian aging and longevity control. NPJ Syst
1000 Biol Appl. 2016;2: 16018.
1001 59. Tyshkovskiy A, Ma S, Shindyapina AV, Tikhonov S, Lee S-G, Bozaykut P, et al. Distinct
1002 longevity mechanisms across and within species and their association with aging. Cell.
1003 2023;186: 2929-2949.e20.
1004 60. McNamara RK, Liu Y, Jandacek R, Rider T, Tso P. The aging human orbitofrontal
1005 cortex: decreasing polyunsaturated fatty acid composition and associated increases in
1006 lipogenic gene expression and stearoyl-CoA desaturase activity. Prostaglandins Leukot
1007 Essent Fatty Acids. 2008;78: 293–304.
1008 61. Hamilton LK, Moquin-Beaudry G, Mangahas CL, Pratesi F, Aubin M, Aumont A, et al.
1009 Stearoyl-CoA Desaturase inhibition reverses immune, synaptic and cognitive
1010 impairments in an Alzheimer's disease mouse model. Nat Commun. 2022;13: 2061.
1011 62. Xu G, Herzig M, Rotrekl V, Walter CA. Base excision repair, aging and health span.
1012 Mech Ageing Dev. 2008;129: 366–382.
1013 63. Debès C, Papadakis A, Grönke S, Karalay Ö, Tain LS, Mizi A, et al. Ageing-associated
1014 changes in transcriptional elongation influence longevity. Nature. 2023;616: 814–821.
1015 64. Papantonis A, Antebi A, Partridge L, Beyer A. Age-associated changes in transcriptional
1016 elongation and their effects on homeostasis. Trends Cell Biol. 2025;35: 645–650.
1017 65. Kuro-o M. Klotho and aging. Biochim Biophys Acta. 2009;1790: 1049–1058.
1018 66. Kershenbaum S, Ireland D, Sabry Z, Rabeler C, Shetty V, Aboobaker A, et al. Variation
1019 in phenotype, genotype, and somatic diversity among asexual Schmidtea mediterranea
1020 planarians. iScience. 2025;28: 113035.
1021 67. Ying H, Hayward DC, Klimovich A, Bosch TCG, Baldassarre L, Neeman T, et al. The
1022 role of DNA methylation in genome defense in Cnidaria and other invertebrates. Mol
1023 Biol Evol. 2022;39: msac018.

1024 68. Doshi R, Kinnear E, Chatterjee S, Guha P, Liu Q. Reliable investigation of DNA
1025 methylation using Oxford nanopore technologies. Sci Rep. 2025;15: 15900.
1026 69. Suzuki MM, Bird A. DNA methylation landscapes: provocative insights from
1027 epigenomics. Nat Rev Genet. 2008;9: 465–476.
1028 70. Dixon G, Liao Y, Bay LK, Matz MV. Role of gene body methylation in acclimatization
1029 and adaptation in a basal metazoan. Proc Natl Acad Sci U S A. 2018;115: 13342–
1030 13346.
1031 71. Li CZ, Haghani A, Yan Q, Lu AT, Zhang J, Fei Z, et al. Epigenetic predictors of species
1032 maximum life span and other life-history traits in mammals. Sci Adv. 2024;10:
1033 eadm7273.
1034 72. Rechsteiner C, Morandini F, Kim SJ, Seluanov A, Gorbunova V. Unlocking longevity
1035 through the comparative biology of aging. Nat Aging. 2025;5: 1686–1703.
1036 73. Lemoine M. The evolution of the hallmarks of aging. Front Genet. 2021;12: 693071.
1037 74. Khalturin K, Hemmrich G, Fraune S, Augustin R, Bosch TCG. More than just orphans:
1038 are taxonomically-restricted genes important in evolution? Trends Genet. 2009;25: 404–
1039 413.
1040 75. Bosch TC, Krylow SM, Bode HR, Steele RE. Thermotolerance and synthesis of heat
1041 shock proteins: these responses are present in Hydra attenuata but absent in Hydra
1042 oligactis. Proc Natl Acad Sci U S A. 1988;85: 7927–7931.
1043 76. De Coster W, Rademakers R. NanoPack2: population-scale evaluation of long-read
1044 sequencing data. Bioinformatics. 2023;39: btad311.
1045 77. Guo L, Accorsi A, He S, Guerrero-Hernández C, Sivagnanam S, McKinney S, et al. An
1046 adaptable chromosome preparation methodology for use in invertebrate research
1047 organisms. BMC Biol. 2018;16: 25.
1048 78. David CN, Campbell RD. Cell cycle kinetics and development of Hydra attenuata. I.
1049 Epithelial cells. J Cell Sci. 1972;11: 557–568.
1050 79. Otomo K, Hibi T, Murata T, Watanabe H, Kawakami R, Nakayama H, et al. Multi-point
1051 scanning two-photon excitation microscopy by utilizing a high-peak-power 1042-nm

1052 laser. Anal Sci. 2015;31: 307–313.
1053 80. Chen S. Ultrafast one-pass FASTQ data preprocessing, quality control, and
1054 deduplication using fastp. Imeta. 2023;2: e107.
1055 81. Durand NC, Shamim MS, Machol I, Rao SSP, Huntley MH, Lander ES, et al. Juicer
1056 provides a one-click system for analyzing loop-resolution Hi-C experiments. Cell Syst.
1057 2016;3: 95–98.
1058 82. Dudchenko O, Batra SS, Omer AD, Nyquist SK, Hoeger M, Durand NC, et al. De novo
1059 assembly of the Aedes aegypti genome using Hi-C yields chromosome-length scaffolds.
1060 Science. 2017;356: 92–95.
1061 83. Flynn JM, Hubley R, Goubert C, Rosen J, Clark AG, Feschotte C, et al.
1062 RepeatModeler2 for automated genomic discovery of transposable element families.
1063 Proc Natl Acad Sci U S A. 2020;117: 9451–9457.
1064 84. Kim D, Paggi JM, Park C, Bennett C, Salzberg SL. Graph-based genome alignment and
1065 genotyping with HISAT2 and HISAT-genotype. Nat Biotechnol. 2019;37: 907–915.
1066 85. Shumate A, Salzberg SL. Liftoff: accurate mapping of gene annotations. Bioinformatics.
1067 2021;37: 1639–1643.
1068 86. Li H. Minimap2: pairwise alignment for nucleotide sequences. Bioinformatics. 2018;34:
1069 3094–3100.
1070 87. Haas BJ. In: https://github.com/transdecoder/transdecoder.
1071 88. Liu H, Steenwyk JL, Zhou X, Schultz DT, Kocot KM, Shen X-X, et al. A taxon-rich and
1072 genome-scale phylogeny of Opisthokonta. PLoS Biol. 2024;22: e3002794.
1073 89. Whelan S, Irisarri I, Burki F. PREQUAL: detecting non-homologous characters in sets of
1074 unaligned homologous sequences. Bioinformatics. 2018;34: 3929–3930.
1075 90. Katoh K, Standley DM. MAFFT multiple sequence alignment software version 7:
1076 improvements in performance and usability. Mol Biol Evol. 2013;30: 772–780.
1077 91. Ali RH, Bogusz M, Whelan S. Identifying clusters of high confidence homologies in
1078 multiple sequence alignments. Mol Biol Evol. 2019;36: 2340–2351.
1079 92. Capella-Gutiérrez S, Silla-Martínez JM, Gabaldón T. trimAl: a tool for automated

1080 alignment trimming in large-scale phylogenetic analyses. Bioinformatics. 2009;25:
1081 1972–1973.
1082 93. Minh BQ, Schmidt HA, Chernomor O, Schrempf D, Woodhams MD, von Haeseler A, et
1083 al. IQ-TREE 2: New models and efficient methods for phylogenetic inference in the
1084 genomic era. Mol Biol Evol. 2020;37: 1530–1534.
1085 94. Ou S, Su W, Liao Y, Chougule K, Agda JRA, Hellinga AJ, et al. Benchmarking
1086 transposable element annotation methods for creation of a streamlined, comprehensive
1087 pipeline. Genome Biol. 2019;20: 275.
1088 95. Gel B, Serra E. karyoploteR: an R/Bioconductor package to plot customizable genomes
1089 displaying arbitrary data. Bioinformatics. 2017;33: 3088–3090.
1090 96. Danecek P, Bonfield JK, Liddle J, Marshall J, Ohan V, Pollard MO, et al. Twelve years
1091 of SAMtools and BCFtools. Gigascience. 2021;10. doi:10.1093/gigascience/giab008
1092 97. Quinlan AR, Hall IM. BEDTools: a flexible suite of utilities for comparing genomic
1093 features. Bioinformatics. 2010;26: 841–842.
1094 98. DeBiasse MB, Buckenmeyer A, Macrander J, Babonis LS, Bentlage B, Cartwright P, et
1095 al. A cnidarian phylogenomic tree fitted with hundreds of 18S leaves. bioRxiv. bioRxiv;
1096 2022. doi:10.1101/2022.10.03.510641
1097 99. Schultz DT, Haddock SHD, Bredeson JV, Green RE, Simakov O, Rokhsar DS. Ancient
1098 gene linkages support ctenophores as sister to other animals. Nature. 2023;618: 110–
1099 117.
1100 100. Yu G, He Q-Y. ReactomePA: an R/Bioconductor package for reactome pathway
1101 analysis and visualization. Mol Biosyst. 2016;12: 477–479.
1102 101. Carlson M, Falcon S, Pages H, Li N. org. Hs. eg. db: Genome wide annotation for
1103 Human. R package version. 2019;3: 3.

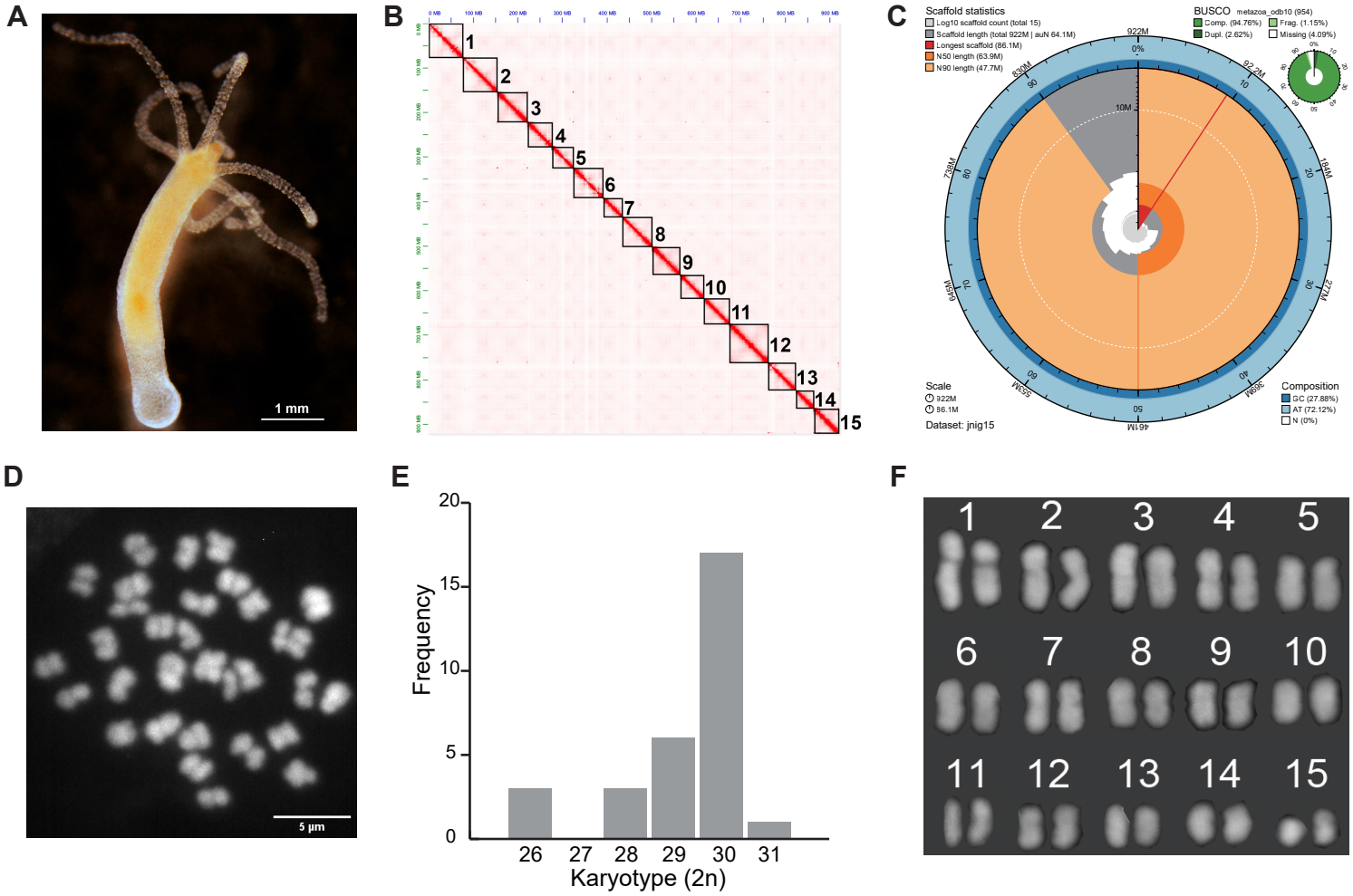

Nojiri, Kin *et al*. Figure 1

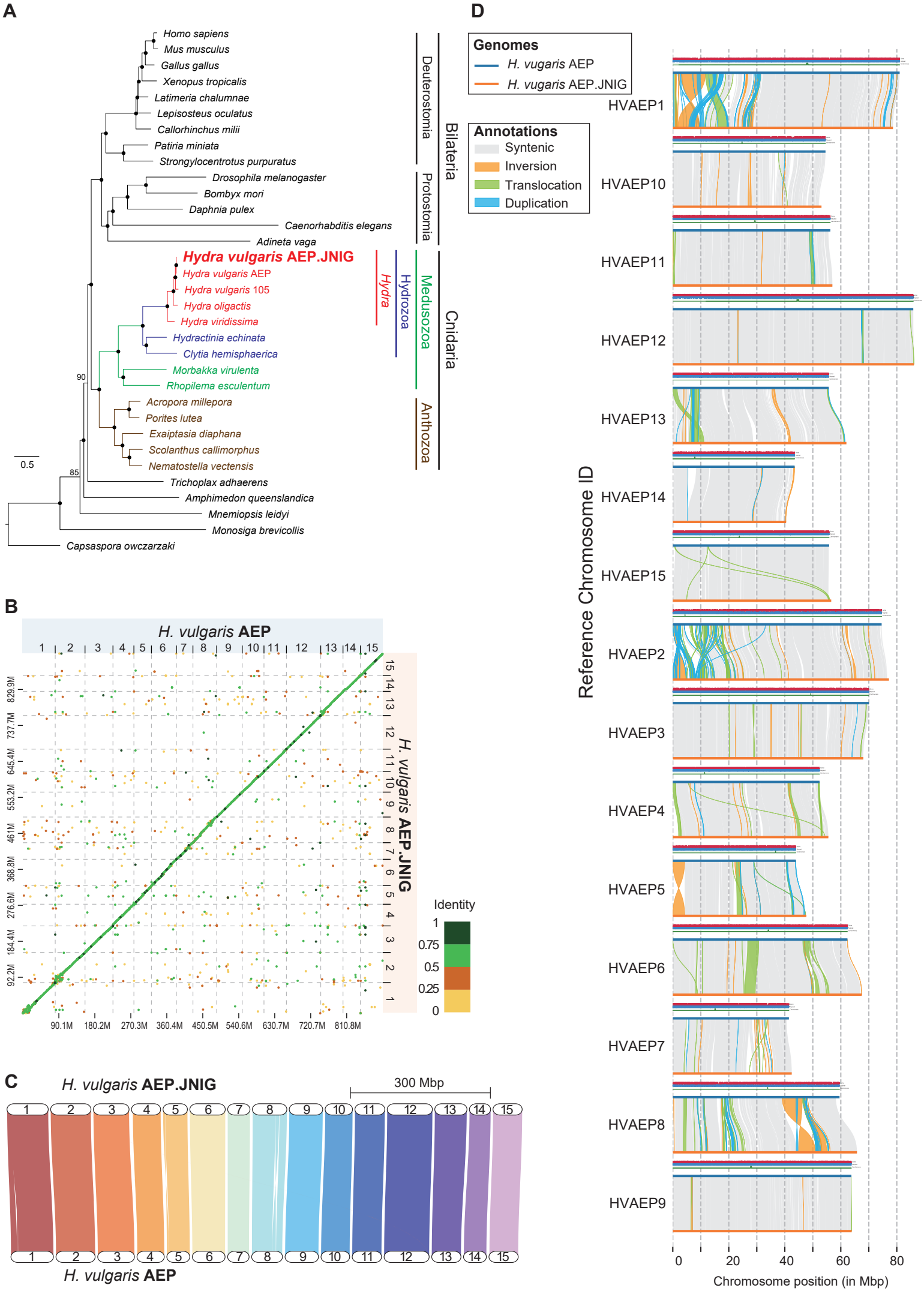

Nojiri, Kin *et al*. Figure 2

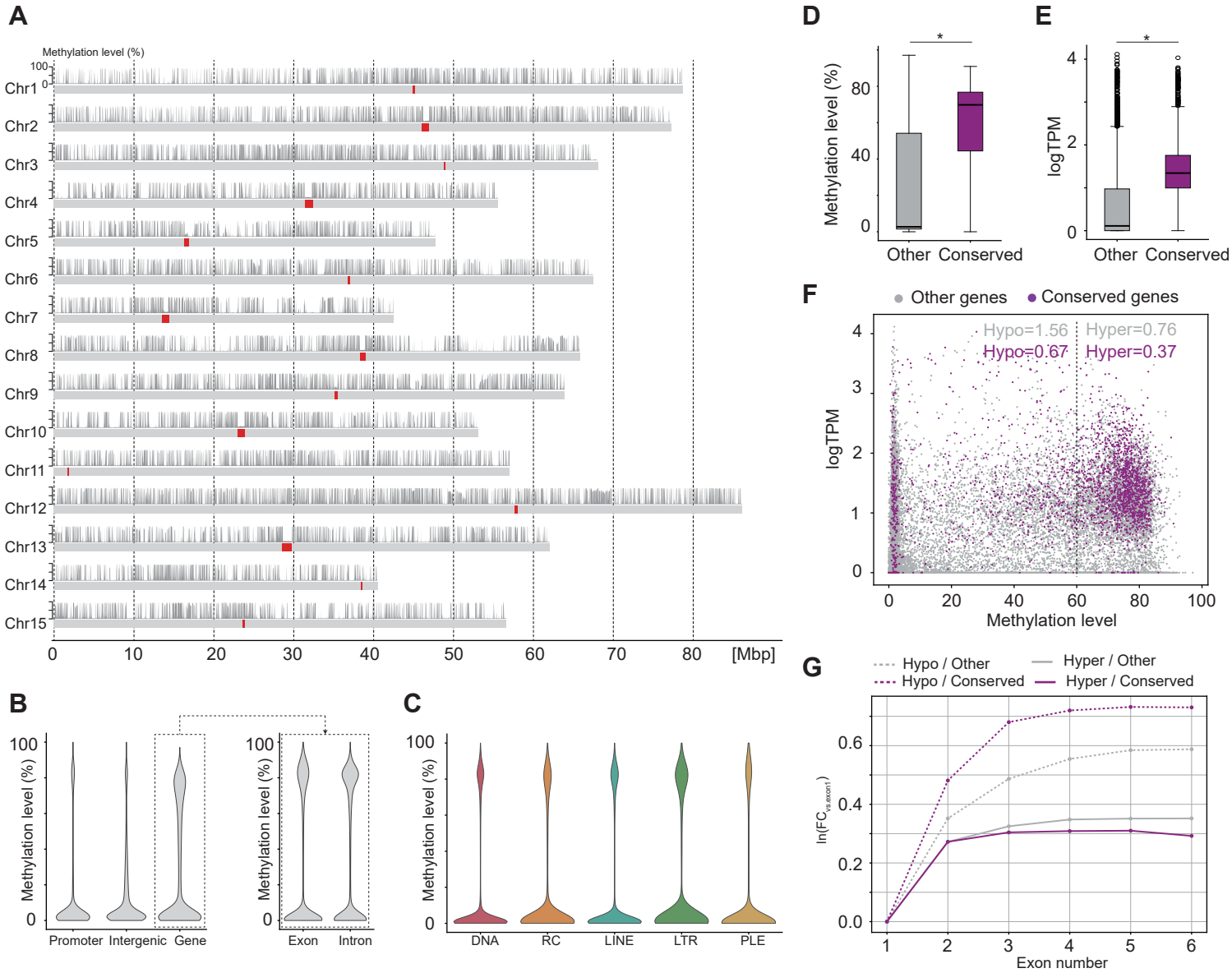

Nojiri, Kin *et al*. Figure 3

A

	H. sapiens	M. musculus	D. melanogasater	C. elegans	H. oligactis	H.vulgaris
hsa03050: proteasome	38	38	36	35	36	36
hsa03083: polycomb repressive complex	40	40	39	34	37	37
hsa03410: base excision repair	42	42	32	27	39	38
hsa03420: nucleotide excision repair	56	56	53	52	55	54
hsa03430: Mismatch repair	22	22	20	19	21	21
hsa03440: Homologous recombination	37	37	26	25	33	33
hsa03450: Non-homologous end-joining	11	11	8	8	11	11
hsa04010: MAPK signaling pathway	134	134	113	105	113	112
hsa04014: Ras signaling pathway	104	104	91	86	92	92
hsa04120: Ubiquitin mediated proteolysis	105	104	100	96	103	103
hsa04137: mitophagy	67	67	62	61	62	64
hsa04140: autophagy	115	115	108	101	107	107
hsa04142: lysosome	90	90	79	77	84	84
hsa04151: PI3K-Akt signaling pathway	173	173	125	119	128	128
hsa04152: AMPK signaling pathway	72	72	68	64	69	68
hsa04211: longevity regulating pathway	51	51	51	46	50	49
hsa04218: Cellular senescence	82	82	74	68	75	75
hsa04310: Wnt signaling pathway	86	86	78	70	80	80
hsa04330: Notch signaling pathway	31	31	28	28	27	27
hsa04340: Hedgehog signaling pathway	35	35	31	30	34	34
hsa04350: TGFβ signaling pathway	58	58	46	48	52	52
hsa04550: Signaling pathways regulating pluripotency of stem cells	60	60	59	58	58	58
hsa04620: Toll-like receptor signaling pathway	53	53	32	31	37	36

B

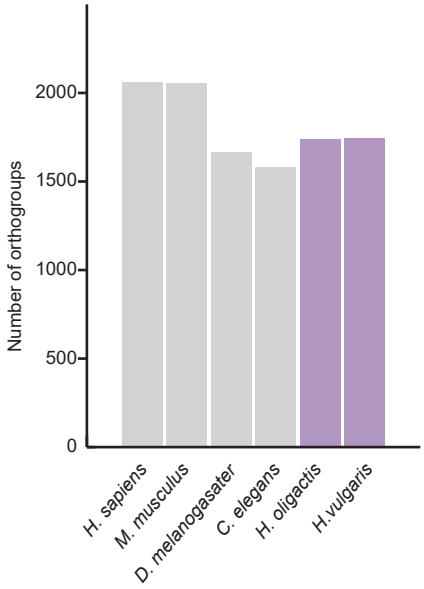

Nojiri, Kin *et al*. Figure 4

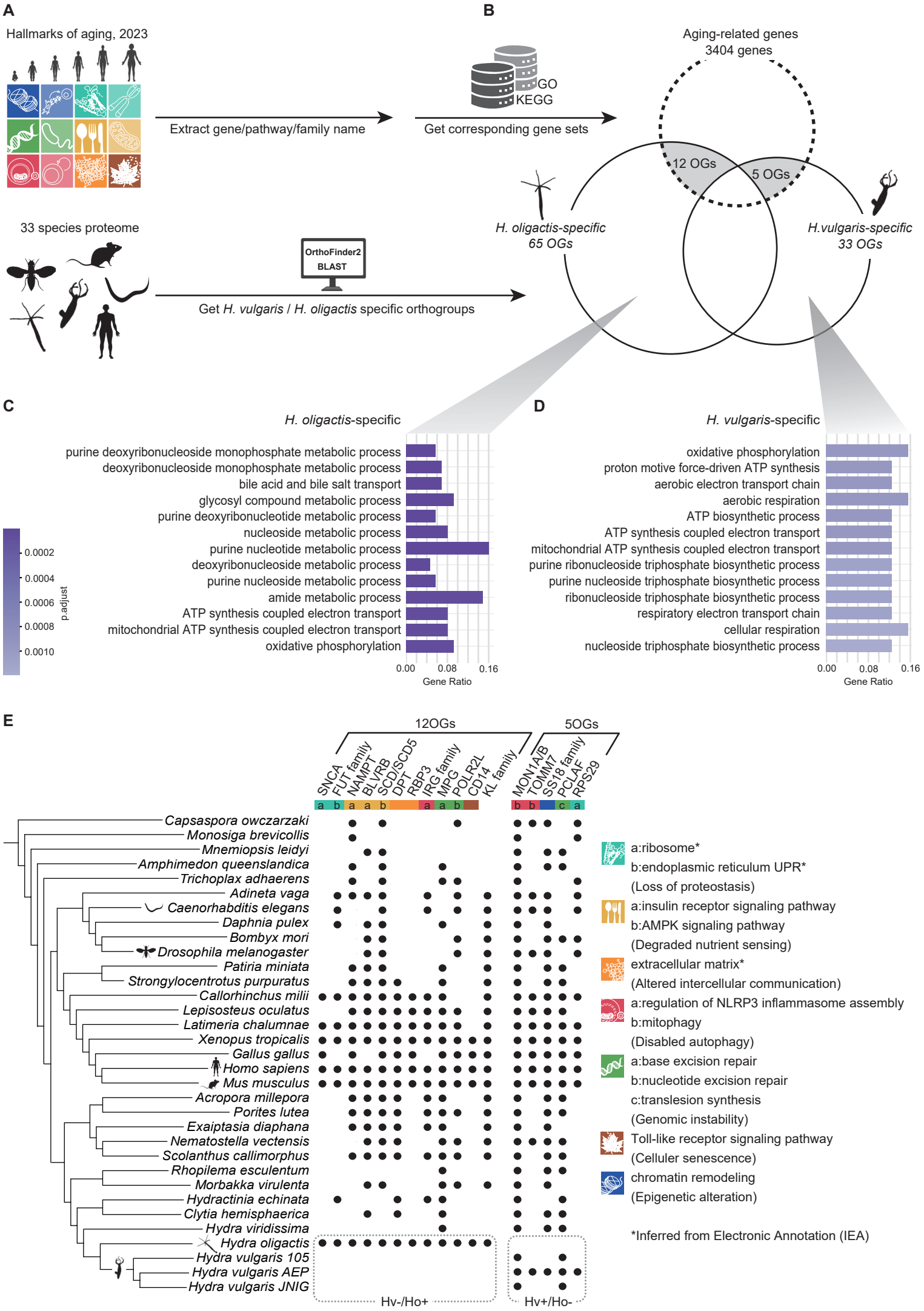

Nojiri, Kin *et al*. Figure 5

Table 1. Summary statistics of the genome sequencing

	Total read	Total base	Read length (N50)
WGS (Illumina)	548,373,038	82,804,238,738	2x150
WGS (Nanopore)	63,239,530	168,380,136,564	3493.0
Hi-C (Illumina)	796,383,332	119,457,499,800	2x150

Table 2. Assembly statistics of the *H. vulgaris* genomes

QUAST v5.3.0	Initial assembly AEP.JNIG	Final Assembly AEP.JNIG	Published Assembly AEP (Cazet *et al*. 2023)
Total length	954,340,183	922,069,947	900,935,055
Scaffolds	248	15	15
Longest scaffold	61,504,050	86,117,336	85,887,368
N50	9,577,232	63,895,935	59,555,380
L50	30	7	7
GC content	27.94	27.88	27.77

Table 3. BUSCO scores of the *H. vulgaris* genome assemblies

BUSCO v5.8.3	Initial assembly AEP.JNIG	Final assmbly AEP.JNIG	Published Assembly AEP (Cazet *et al*. 2023)
Complete BUSCOs	889 (93.2%)	904 (94.7%)	906 (95%)
Complete and single-copy BUSCOs	820 (86.0%)	879 (92.1%)	893 (93.6%)
Complete and duplicated BUSCOs	69 (7.2%)	25 (2.6%)	13 (1.4%)
Fragmented BUSCOs	26 (2.7%)	11 (1.2%)	11 (1.2%)
Missing BUSCOs	39 (4.1%)	39 (4.1%)	37 (3.9%)
Total BUSCO group searched	954	954	954

Table 4. BUSCO scores of the gene models based on the chromosome-level genome assemblies

BUSCO v5.8.3	Final assmbly AEP.JNIG	Published Assembly AEP (Cazet *et al*. 2023)
Complete BUSCOs	891 (93.4%)	905 (94.9%)
Complete and single-copy BUSCOs	772 (80.9%)	705 (73.9%)
Complete and duplicated BUSCOs	119 (12.5%)	200 (21.0%)
Fragmented BUSCOs	14 (1.5%)	14 (1.5%)
Missing BUSCOs	49 (5.1%)	35 (3.7%)
Total BUSCO group searched	954	954

Table 5. Composition of TEs identified by Earl Grey in the genome of *H. vulgaris* AEP.JNIG

TE Classification	Coverage (bp)	Copy number	% Genome coverage	Genome size	TE family count
DNA	330,098,105	597,308	35.8	922,069,947	597,307
Rolling Circle	8,793,916	19,836	0.954	922,069,947	19,836
Penelope	23,760,322	68,248	2.58	922,069,947	68,248
LINE	140,003,727	267,317	15.2	922,069,947	267,317
LTR	9,088,772	10,622	0.986	922,069,947	10,622
Other (Simple Repeat, Microsatellite, RNA)	54,617,458	421,636	5.92	922,069,947	421,636
Unclassified	156,717,139	504,751	17.0	922,069,947	504,750
Repeat	723,079,439	NA	78.4	922,069,947	NA
Non-Repeat	198,990,508	NA	21.6	922,069,947	NA

Table 6. Composition of TEs identified by Earl Grey in the genome of *H. vulgaris* AEP

TE Classification	Coverage (bp)	Copy number	% Genome coverage	Genome size	TE family count
DNA	325,041,912	583,293	36.1	900,935,055	583,293
Rolling Circle	8,786,864	18,840	0.975	900,935,055	18,840
Penelope	20,973,039	55,171	2.33	900,935,055	55,171
LINE	138,121,823	244,363	15.3	900,935,055	244,363
LTR	9,180,297	12,122	1.02	900,935,055	12,122
Other (Simple Repeat, Microsatellite, RNA)	51,236,873	418,879	5.69	900,935,055	418,877
Unclassified	146,461,074	459,730	16.3	900,935,055	459,730
Repeat	699,801,882	NA	77.7	900,935,055	NA
Non-Repeat	201,133,173	NA	22.3	900,935,055	NA

Nojiri, Kin *et al*. Tables

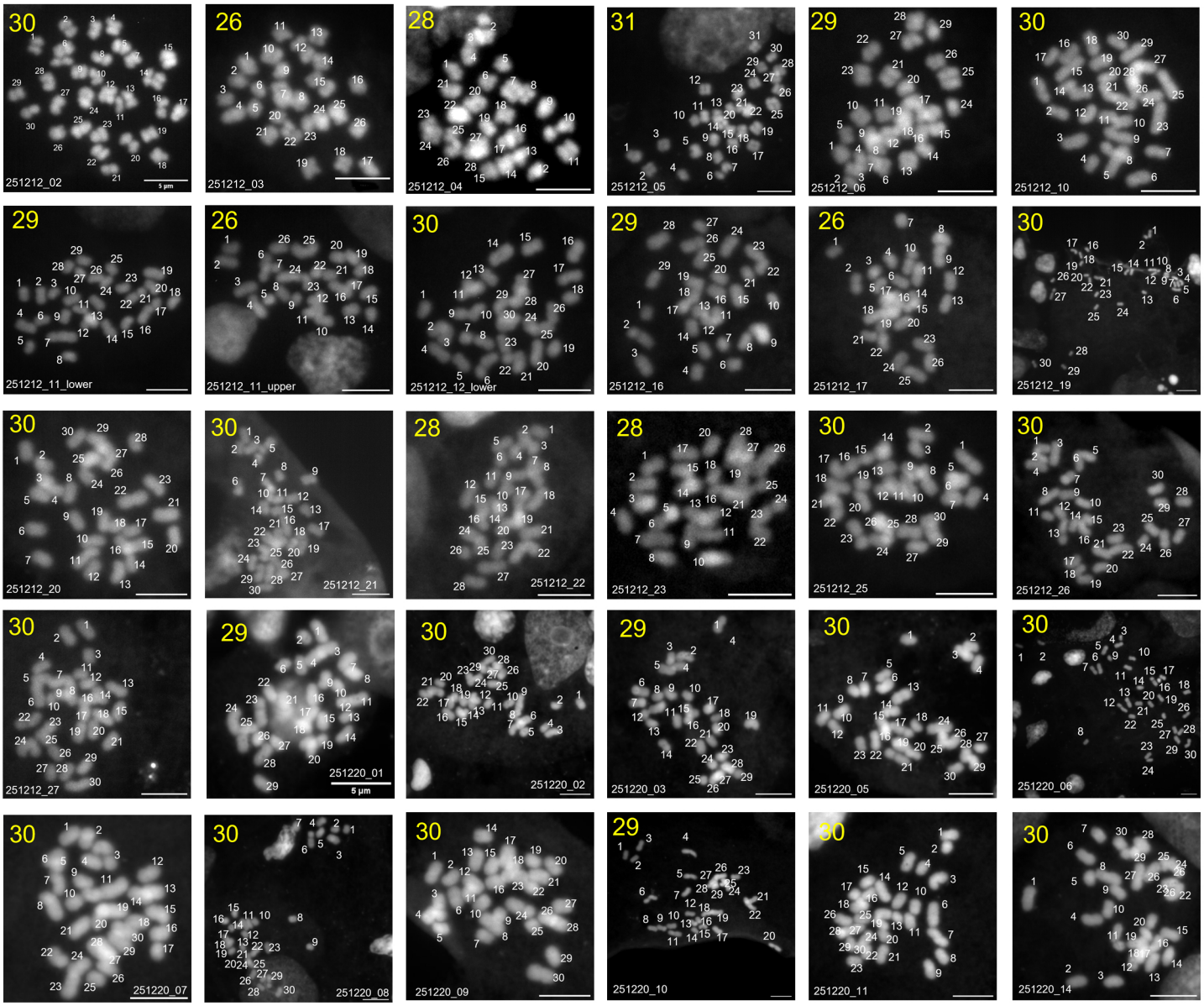

Nojiri, Kin *et al.*, Figure S1

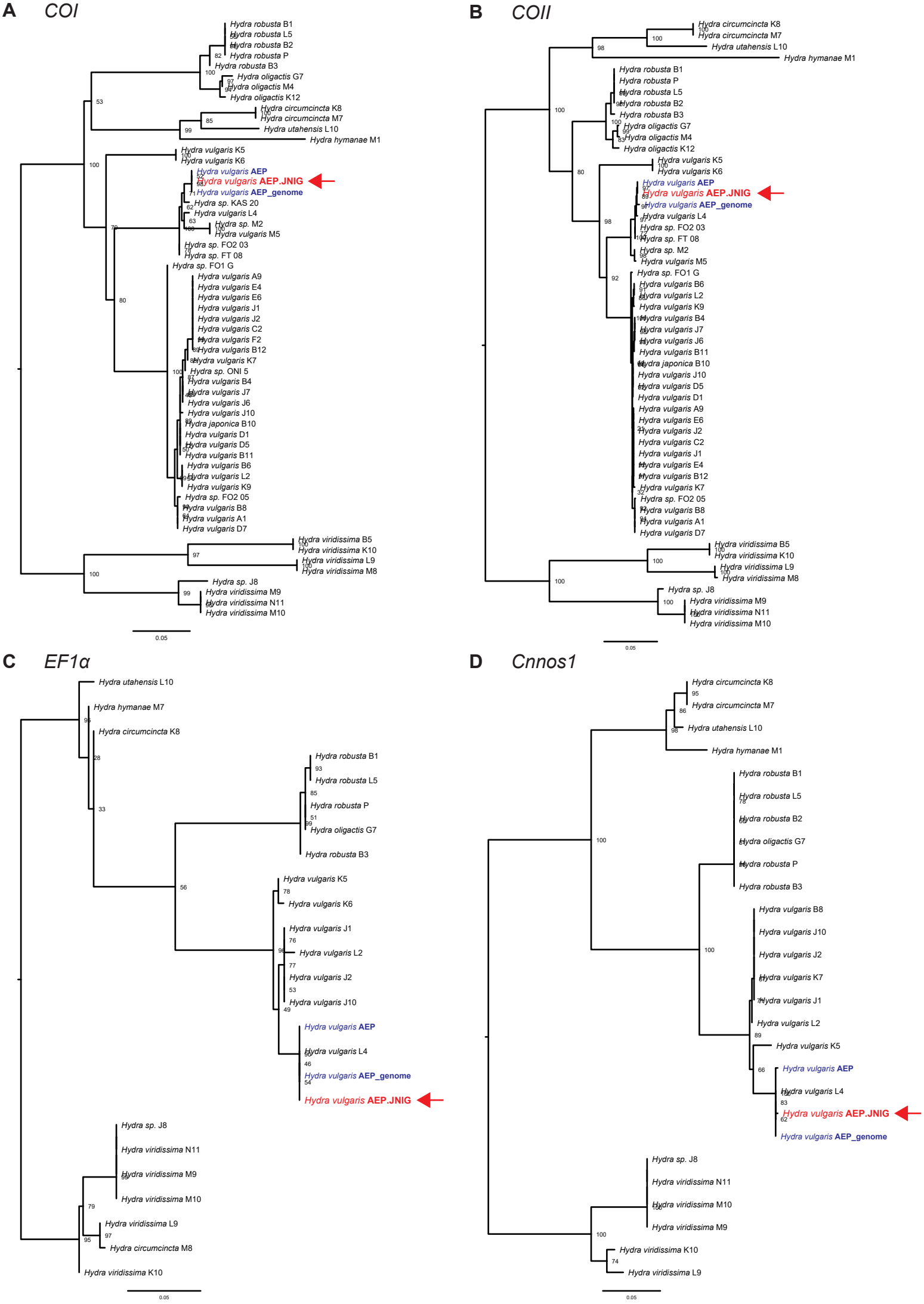

Nojiri, Kin *et al*. Figure S2

A

Structual annotations

Variation type	Counts	Length_ref	Length_qry
Syntenic regions	954	795720877	788696964
Inversions	360	31484124	33524687
Translocations	660	31504935	32468566
Duplications (reference)	239	5965793	-
Duplications (query)	2073	-	14204764
Not aligned (reference)	1591	60624245	-
Not aligned (query)	3516	-	57781185

Sequence annotations

Variation type	Counts	Length_ref	Length_qry
SNPs	1833472	1833472	1833472
Insertions	648211	-	5429694
Deletions	261207	4662625	-
Copy gains	119	-	2375861
Copy losses	129	1112463	-
Highly diverged	27555	125424357	119430308
Tandem repeats	369	87143	77078

B

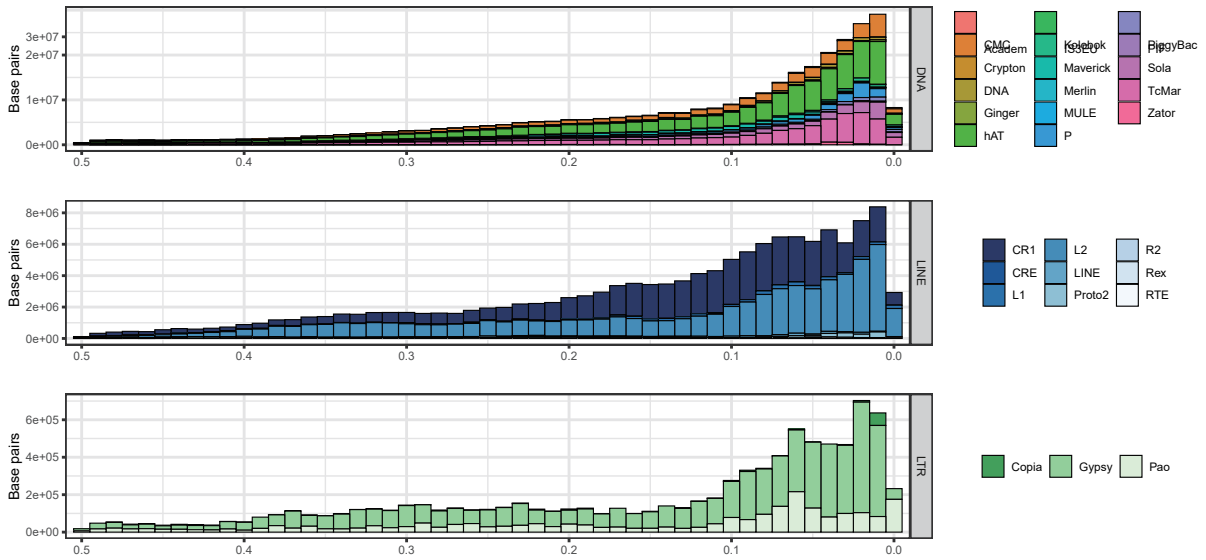

C

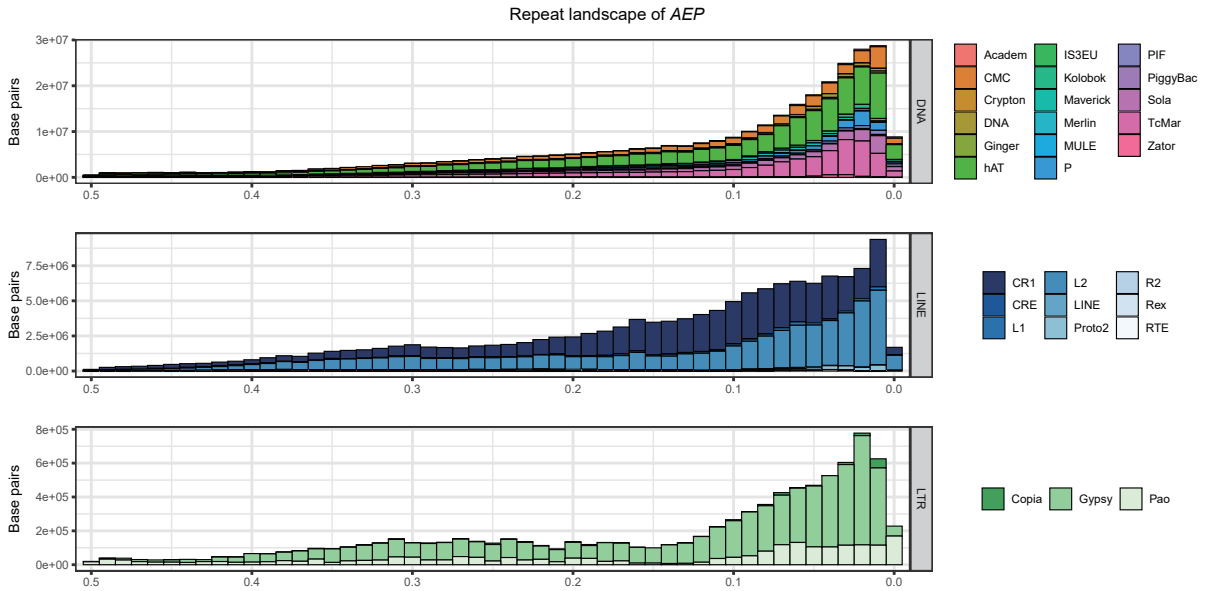

Nojiri, Kin *et al*. Figure S3

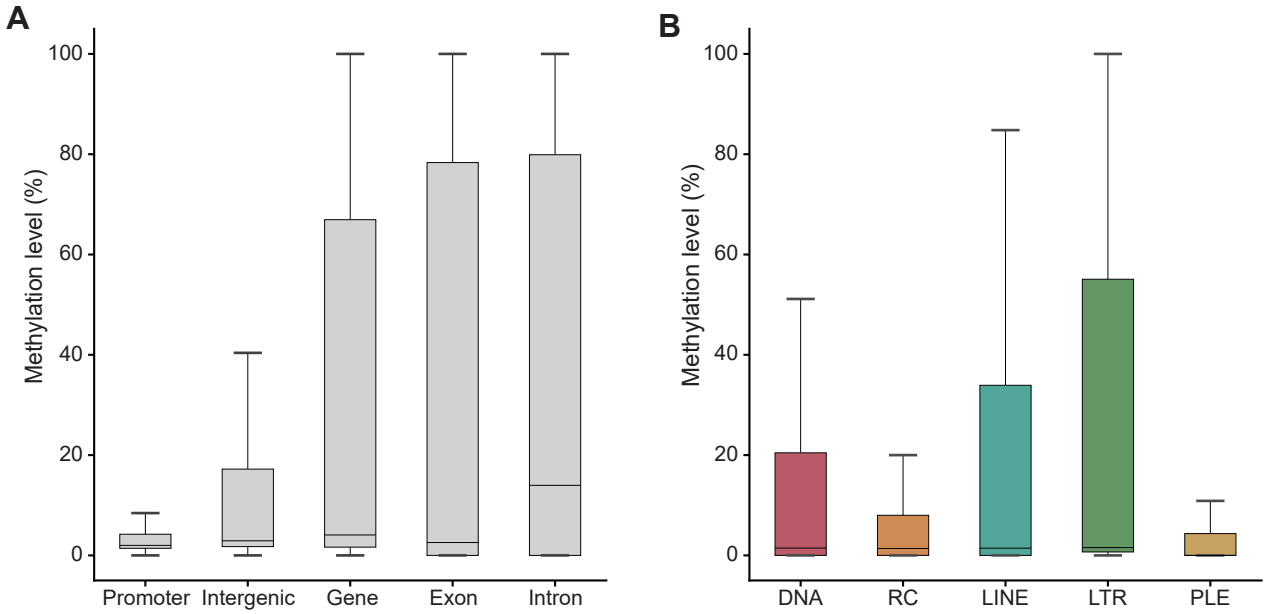

Nojiri, Kin *et al*. Figure S4

	H. sapiens	M. musculus	D. melanogasater	C. elegans	H. oligactis	H.vulgaris
GO:0004402 histone acetyltransferase activity	29	29	27	26	28	28
GO:0004407 histone deacetylase activity	11	11	11	10	11	11
GO:0005125 cytokine activity	134	133	24	30	36	35
GO:0005840 ribosome	206	206	200	191	189	189
GO:0006338 chromatin remodeling	434	434	378	335	392	393
GO:0008286 insulin receptor signaling pathway	61	61	58	55	58	56
GO:0008459 chondroitin 6-sulfotransferase activity	1	1	1	0	1	1
GO:0009008 DNA-methyltransferase activity	4	4	4	3	4	4
GO:0019985 translesion synthesis	23	23	19	18	21	22
GO:0030968 endoplasmic reticulum unfolded protein response	59	59	52	49	55	54
GO:0031012 extracellular matrix	237	237	174	169	189	187
GO:0031445 regulation of heterochromatin formation	9	9	8	8	9	9
GO:0031577 spindle checkpoint signaling	29	29	22	23	28	28
GO:0031931 TORC1 complex	6	6	6	5	6	6
GO:0032200 telomere organization	101	101	82	72	92	92
GO:0032452 histone demethylase activity	13	13	13	11	13	13
GO:0038084 vascular endothelial growth factor signaling pathway	13	13	13	10	13	13
GO:0040029 epigenetic regulation of gene expression	200	200	169	147	175	175
GO:0042054 histone methyltransferase activity	35	35	33	32	34	34
GO:0045814 negative regulation of gene expression	128	128	107	94	113	113
GO:0046902 regulation of mitochondrial membrane permeability	43	43	34	31	36	36
GO:0097472 cyclin dependent protein kinase activity	12	12	12	12	12	12
GO:0140807 NAD protein glutamate ADP ribosyltransferase activity	6	6	6	5	6	6
GO:0140896 cGAS STING signaling pathway	28	28	26	26	26	26
GO:0141137 positive regulation of gene expression	48	48	44	38	44	44
GO:1900225 regulation of NLRP3 inflammasome complex assembly	45	45	37	38	39	38

Nojiri, Kin *et al*. Figure S5

H. oligactis specifc orthogroups

H. vulgaris specifc orthogroups

A

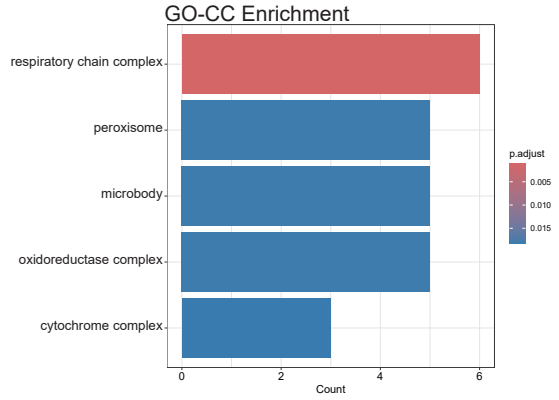

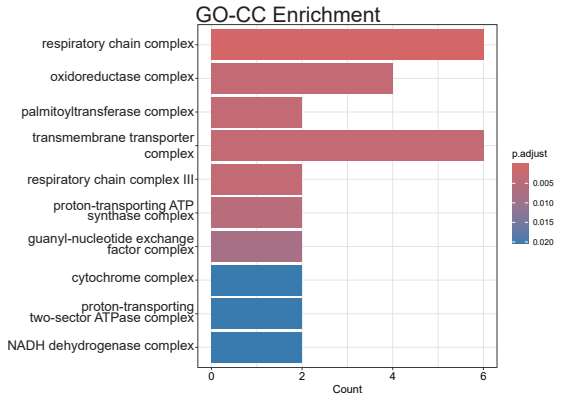

B

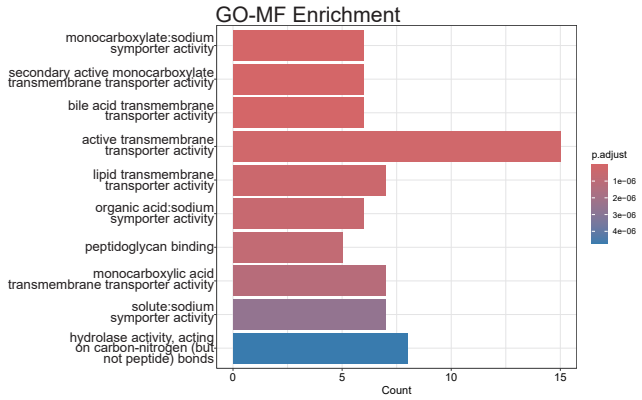

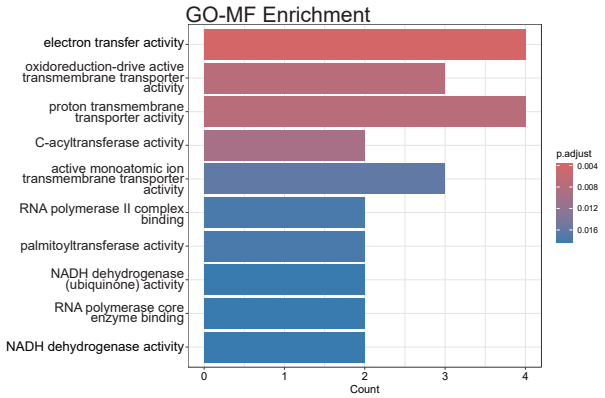

C

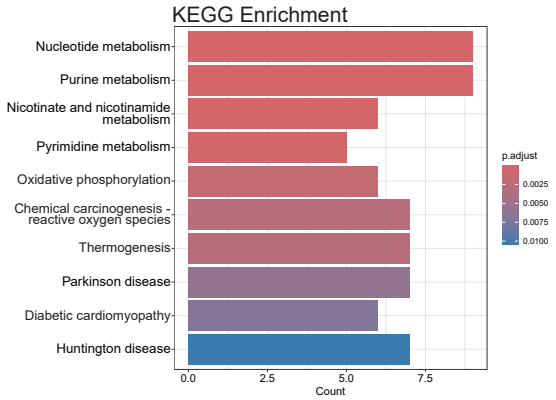

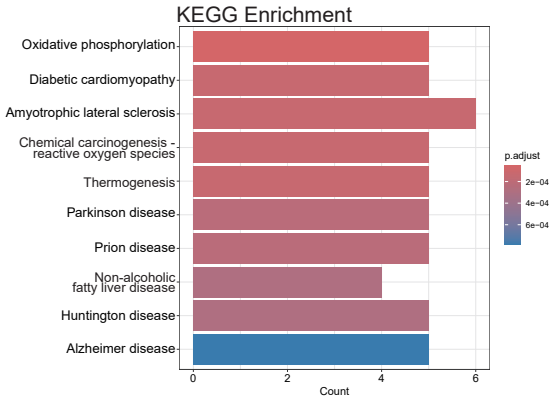

D

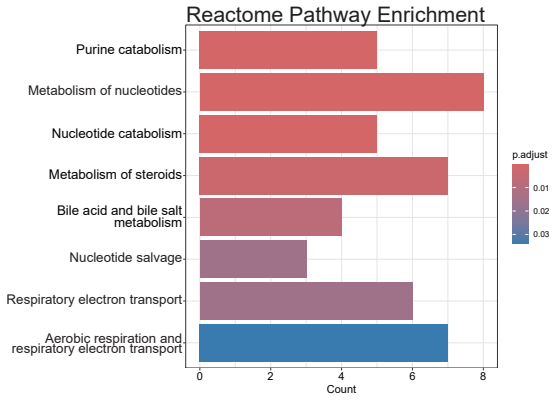

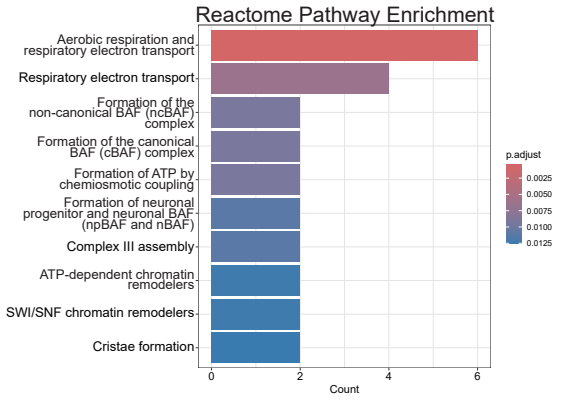

Nojiri, Kin *et al*. Figure S6